# Comprehensive fitness landscape of SARS-CoV-2 $M^{pro}$ reveals insights into viral resistance mechanisms

Julia M. Flynn[1,#], Neha Samant[1], Gily Schneider-Nachum[1], David T. Barkan[2], Nese Kurt Yilmaz[1], Celia A. Schiffer[1], Stephanie A. Moquin[2], Dustin Dovala[2], and Daniel N.A. Bolon[1,#]

[1]Department of Biochemistry and Molecular Biotechnology

University of Massachusetts Chan Medical School

Worcester, MA 01605, USA

[2]Novartis Institutes for Biomedical Research

Emeryville, CA 94608, USA

[#] corresponding authors, Julia.Flynn@umassmed.edu, Dan.Bolon@umassmed.edu

## Abstract

With the continual evolution of new strains of SARS-CoV-2 that are more virulent, transmissible, and able to evade current vaccines, there is an urgent need for effective anti-viral drugs. SARS-CoV-2 main protease ($M^{pro}$) is a leading target for drug design due to its conserved and indispensable role in the viral life cycle. Drugs targeting $M^{pro}$ appear promising but will elicit selection pressure for resistance. To understand resistance potential in $M^{pro}$, we performed a comprehensive mutational scan of the protease that analyzed the function of all possible single amino acid changes. We developed three separate high-throughput assays of $M^{pro}$ function in yeast, based on either the ability of $M^{pro}$ variants to cleave at a defined cut-site or on the toxicity of their expression to yeast. We used deep sequencing to quantify the functional effects of each variant in each screen. The protein fitness landscapes from all three screens were strongly correlated, indicating that they captured the biophysical properties critical to $M^{pro}$ function. The fitness landscapes revealed a non-active site location on the surface that is extremely sensitive to mutation making it a favorable location to target with inhibitors. In addition, we found a network of critical amino acids that physically bridge the two active sites of the $M^{pro}$ dimer. The clinical variants of $M^{pro}$ were predominantly functional in our screens, indicating that $M^{pro}$ is under strong selection pressure in the human population. Our results provide predictions of mutations that will be readily accessible to $M^{pro}$ evolution and that are likely to contribute to drug resistance. This complete mutational guide of $M^{pro}$ can be used in the design of inhibitors with reduced potential of evolving viral resistance.

# Introduction

The COVID-19 pandemic, caused by the Severe Acute Respiratory Syndrome Coronavirus-2 (SARS-CoV-2), has had an unprecedented impact on global health, the world economy, and our overall way of life. Despite the rapid deployment of mRNA and traditional vaccines against SARS-CoV-2 which have served to greatly improve patient outcome and decrease spread of the disease, vaccines remain unavailable in many parts of the world and there is hesitancy to get vaccinated among portions of the population. Additionally, the virus appears to be evolving mutations in the Spike protein that reduce immune protection from both vaccines and prior infections. Additional strategies including direct-acting antiviral drugs are needed to combat the SARS-CoV-2 pandemic. The main protease ($M^{pro}$) of SARS-CoV-2 is a promising target for drug development with many laboratories working collaboratively to develop drugs against this protease, leading to thousands of $M^{pro}$ inhibitors in the pipeline and the first FDA-authorized clinical drug against this target. The use of drugs that target $M^{pro}$ will apply selection pressure for the evolution of resistance. There is potential to design drugs with reduced likelihood of developing $M^{pro}$ resistance, but these efforts will require an in-depth understanding of the evolutionary potential of the protease.

SARS-CoV-2 is a highly contagious virus responsible for the ongoing COVID-19 pandemic. SARS-CoV-2 belongs to the group of coronaviruses and has a positive-sense single-stranded RNA genome. Immediately upon entry into the host cell, the SARS-CoV-2 virus translates its replicase gene (ORF1) into two overlapping large polyproteins produced in tandem by a ribosomal frameshift, pp1a and pp1ab. These polyproteins are cleaved by two cysteine proteases, $M^{pro}$ (also known as the chymotrypsin-like protease, $3CL^{pro}$, or Nsp5) and the papain-like protease ($PL^{pro}$) to yield functional replication machinery indispensable to viral replication. $M^{pro}$ initiates autoproteolysis from the pp1a and pp1ab polypeptides at its N- and C- terminus, through a poorly understood mechanism. Subsequently, mature $M^{pro}$ cuts at 11 additional cleavage sites in both pp1a and pp1ab. The sites cut by $M^{pro}$ all include a conserved Gln at the P1 position, a small amino acid (Ser, Ala or Gly) at the P1' position, and a hydrophobic residue (Leu, Phe, or Val) at the P2 position (Hegyi, Friebe et al. 2002, Thiel, Ivanov et al. 2003). Along with its vital role in the liberation of viral proteins, $M^{pro}$ also cleaves specific host proteins, an activity which has been shown to enhance viral replication (Meyer, Chiaravalli et al. 2021). Through its substrates, $M^{pro}$ function is required for almost every known step in the viral life cycle.

$M^{pro}$ is a highly attractive target for drug development against SARS-CoV-2 and future coronavirus-mediated pandemics for numerous reasons. $M^{pro}$ plays an essential functional role in the viral life cycle so that blocking its function will impair viral propagation. $M^{pro}$ is highly conserved among all coronaviruses making it likely that inhibitors will have broad efficacy in potential future pandemics.

There are no human $M^{pro}$ homologs, and it shares no overlapping substrate specificity with any known human protease, minimizing the possibility of side effects. Additionally, its nucleophilic cysteine active site enables the design of covalent inhibitors that provide advantages such as increased potency, selectivity, and duration of inhibition (Singh, Petter et al. 2011). For these reasons, $M^{pro}$ has become one of the most characterized SARS-CoV-2 drug targets (Jin, Du et al. 2020, Zhang, Lin et al. 2020, Biering, Van Dis et al. 2021, Fischer, Veprek et al. 2021).

Native $M^{pro}$ is a homodimer, and each monomer is composed of three domains (Jin, Du et al. 2020). Domain I (8-101) and Domain II (102-184) are comprised of antiparallel β-barrel structures. Cys145 and His41 make up $M^{pro}$'s noncanonical catalytic dyad and are located in a cleft between Domains I and II. Domain III (201-303) is an all α-helical domain that coordinates $M^{pro}$ dimerization, which is essential for $M^{pro}$ function (Tan, Verschueren et al. 2005). Much of the structural and enzymatic knowledge of SARS-CoV-2 $M^{pro}$ has been derived from studies of SARS-CoV-1 that caused the 2003 SARS outbreak (Ksiazek, Erdman et al. 2003), as well as MERS-CoV that caused the 2012 MERS outbreak (Zaki, van Boheemen et al. 2012). $M^{pro}$ from SARS-CoV-1 and SARS-CoV-2 differ in sequence at only 12 residues, however SARS-CoV-2 $M^{pro}$ exhibits increased structural flexibility and plasticity (Bzowka, Mitusinska et al. 2020, Estrada 2020, Kneller, Phillips et al. 2020).

We performed comprehensive mutational analysis of SARS-CoV-2 $M^{pro}$ to provide functional and structural information to aid in the design of effective inhibitors against the protease. Systematic mutational scanning assesses the consequences of all point mutations in a gene providing a comprehensive picture of the relationship between protein sequence and function (Hietpas, Jensen et al. 2011, Fowler and Fields 2014). Mutational scanning requires a selection step that separates variants based on function. Following selection, the frequency of each variant is assessed by deep sequencing to estimate functional effects. The resulting protein fitness landscape describes how all individual amino acid changes in a protein impact function and provides a detailed guide of the biophysical properties that underlie fitness. Protein fitness landscapes identify mutation-tolerant positions that may readily contribute to drug resistance. These studies also elucidate mutation-sensitive residues that are critical to function, making them attractive target sites for inhibitors with reduced likelihood of developing resistance. The work described here focuses on fitness landscapes without drug pressure because these provide critical information regarding $M^{pro}$ mechanism and evolutionary potential that we hope will be useful in the efforts to combat SARS-CoV-2. We are pursuing investigations in the presence of inhibitors, but these experiments will require further optimization steps to make our yeast-based assays compatible with inhibition. Of note, mutational scans of other drug targets including lactamases (Deng, Huang et al. 2012, Firnberg, Labonte et al. 2014) and oncogenes (Choi, Landrette et al. 2014, Ma, Boucher et al. 2017) have demonstrated the potential to accurately identify and predict clinically-relevant resistance evolution.

In this study, we used systematic mutational scanning to analyze the functional effects of every individual amino acid change in $M^{pro}$. We developed three orthogonal screens in yeast to separate $M^{pro}$ variants based on function (Figure 1). The first screen measures $M^{pro}$ activity via loss of Fluorescence Resonance Energy Transfer (FRET) from a genetically-encoded FRET pair linked by the Nsp4/5 cleavage sequence. The second screen similarly measures cleavage of the Nsp4/5 cut site; however, in this screen $M^{pro}$ cleavage leads to inactivation of a transcription factor driving GFP expression. The final screen leverages the toxicity of wild-type (WT) $M^{pro}$ to yeast, which leads to depletion of active variants during growth. Following selection in the three screens, populations were subjected to deep sequencing in order to quantify function based on the enrichment or depletion of each variant.

We found that the functional scores between screens were correlated, indicating that they all captured key biophysical properties governing function. Our functional scores also correlated well with previously measured catalytic rates of purified individual mutants. Additionally, substitutions in $M^{pro}$ from coronaviruses distantly related to SARS-CoV-2 consistently exhibited high function in our screens indicating that similar biophysical properties underlie the function of genetically-diverse $M^{pro}$ sequences. Our study revealed mutation-sensitive sites distal to the active site and dimerization interface. These allosteric sites reveal important communication networks that may be targeted by inhibitors. Our results provide a comprehensive dataset which can be used to design molecules with decreased vulnerability to resistance, by building drug-protein interactions at mutation-sensitive sites while avoiding mutation-tolerant residues.

## Results

### Expression of mature WT $M^{pro}$ in yeast

The main protease of SARS-CoV-2 is produced by self-cleavage of polyproteins translated from the viral RNA genome, and its enzymatic activity is inhibited by the presence of additional N- and C-terminal amino acids (Xue, Yang et al. 2007). To express $M^{pro}$ with its authentic N-terminal serine residue, we generated a Ubiquitin-$M^{pro}$ fusion protein. In yeast and other eukaryotes, Ubiquitin (Ub) fusion proteins are cleaved by Ub-specific proteases directly C-terminal to the Ub, revealing the N-terminal residue of the fused protein, regardless of sequence (Bachmair, Finley et al. 1986). Expression of functionally-active $M^{pro}$ is toxic to yeast

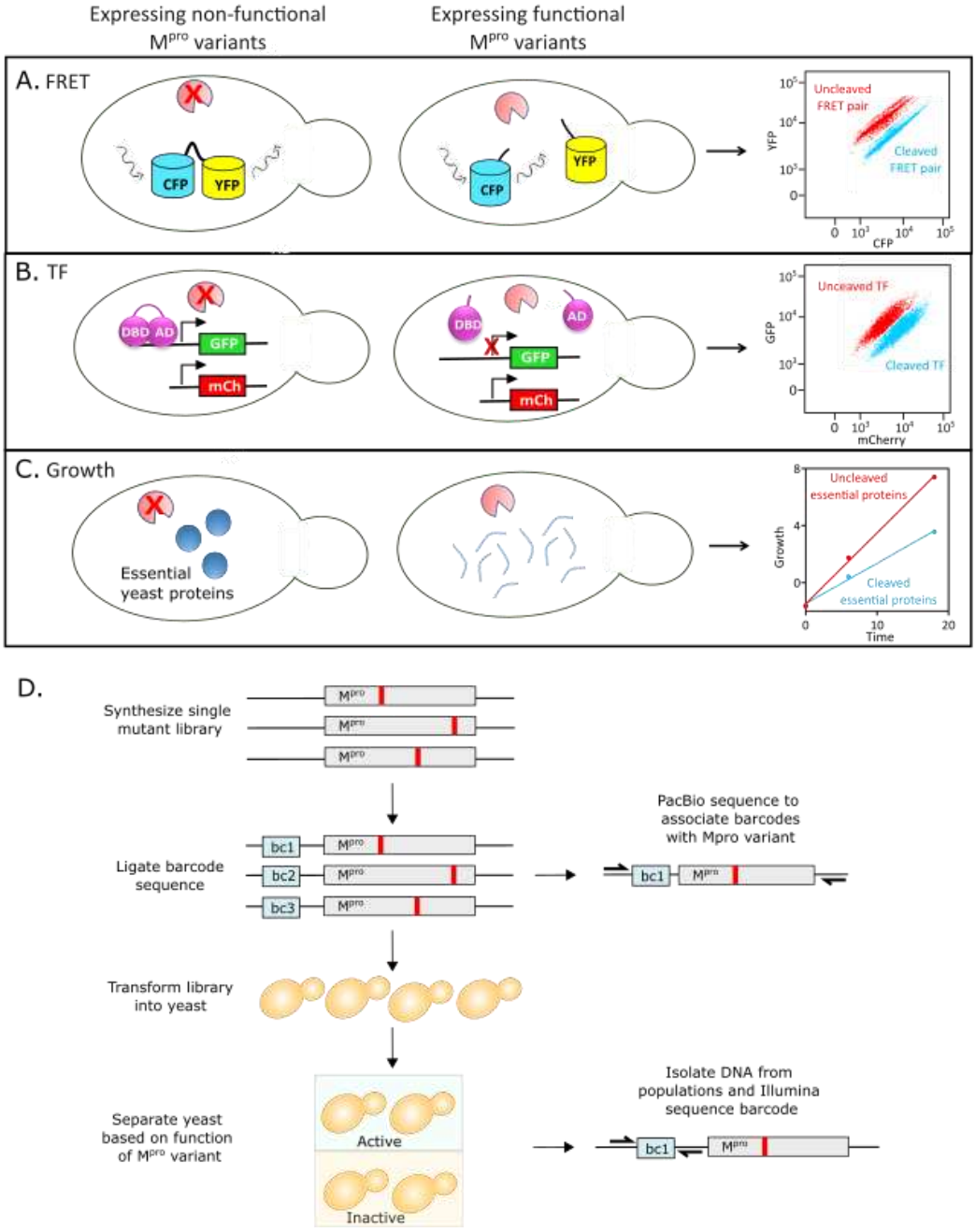


**Figure 1. Experimental strategy to measure the function of all individual mutations of M$^{pro}$.** A. FRET-based reporter screen. M$^{pro}$ variants were sorted based on their ability to cleave at the M$^{pro}$ cut-site, separating the YFP-CFP FRET pair. Cells were separated by FACS into cleaved (low FRET) and uncleaved (high FRET) populations. B. Split transcription factor screen. M$^{pro}$ variants were sorted based on their ability to cleave at the M$^{pro}$ cut-site, separating the DNA binding domain (DBD) and activation domain (AD) of the Gal4 transcription factor. The transcription factor drives GFP expression from a galactose promoter. Cells were separated by FACS into cleaved (low GFP expression) and uncleaved (high GFP expression) populations. C. Growth screen. Yeast cells expressing functional M$^{pro}$ variants that cleave essential yeast proteins grow slowly and are depleted in bulk culture, while yeast cells expressing non-functional M$^{pro}$ variants are enriched. D. Barcoding strategy to measure frequency of all individual mutations of M$^{pro}$ in a single experiment.

cells (Alalam, Sigurdardottir et al. 2021). To control the expression level of $M^{pro}$ while limiting its toxic side effects, we placed Ub-$M^{pro}$ under control of the inducible and engineered LexA-ER-AD transcription factor (Ottoz, Rudolf et al. 2014). LexA-ER-AD is a fusion of the bacterial LexA DNA-binding protein, the human estrogen rector (ER) and the B112 activation domain, and its activity is tightly and precisely regulated by the hormone β-estradiol. We inserted 4 *lexA* boxes recognized by the LexA DNA binding domain upstream of Ub-$M^{pro}$ to control its expression. The Western blot in Figure S1a illustrates both induction of $M^{pro}$ by β-estradiol and successful removal of the Ub moiety, indicating that the protease is being expressed in its mature and functional form. We performed a titration curve with β-estradiol to determine the lowest concentration at which $M^{pro}$ can be expressed without inhibiting yeast cell growth while still enabling measurement of substrate cleavage (Figure S1b).

**Engineering of functional screens to monitor intracellular $M^{pro}$ activity**

We developed three distinct yeast screens to characterize the effects of $M^{pro}$ variants on function (Figure 1). The first screen utilized a FRET-based reporter of two fluorescent proteins, YPet and CyPet, fused together with the Nsp4/5 $M^{pro}$ cleavage site engineered in the middle (YPet-$M^{pro}$CS-CyPet) (Figure 1a). The YPet-CyPet pair are derivatives of the YFP-CFP proteins that have been fluorescently optimized by directed evolution for intracellular FRET (Nguyen and Daugherty 2005) and provide a 20-fold signal change upon cleavage. The linker between the two fluorescent proteins contains the $M^{pro}$ cleavage site, TSAVLQ|SGFRK, the cut-site at the N-terminus of the $M^{pro}$ protease. This is the most commonly used cut-site for *in vitro* cleavage assays, which allowed us to directly compare our mutational results to those that were previously published. One advantage of this assay is that the fluorescent readout directly reports on cleavage of a specific cut-site. The plasmid containing Ub-$M^{pro}$ under the control of β-estradiol was transformed into yeast cells expressing a chromosomally integrated copy of YPet-$M^{pro}$CS-CyPet. Expression of WT $M^{pro}$ led to a β-estradiol-dependent decrease in FRET signal as measured by fluorescence-activated single cell sorting (FACS). Mutation of the essential catalytic cysteine of $M^{pro}$ to alanine (C145A) abolished this change in FRET signal indicating that the change in signal was dependent on the presence of functional $M^{pro}$ (Figure S1c).

The second screen utilized the DNA binding domain and activation domain of the Gal4 transcription factor, separated by the Nsp4/5 cut site (Johnston, Zavortink et al. 1986, Murray, Hung et al. 1993). We used this engineered transcription factor (TF) to drive GFP expression, enabling cells with varying levels of $M^{pro}$ protease activity to be separated by FACS (Figure 1b). One benefit of this system is its signal amplification, as one cut transcription factor can cause a reduction of more than one GFP molecule. However, due to this amplification, the fluorescent signal is indirectly related to cutting efficiency. Expression of Ub-$M^{pro}$ in cells engineered with the split transcriptional factor exhibited a β-estradiol-dependent decrease in GFP reporter activity that required the presence of catalytically-functional $M^{pro}$ protein (Figure S1d).

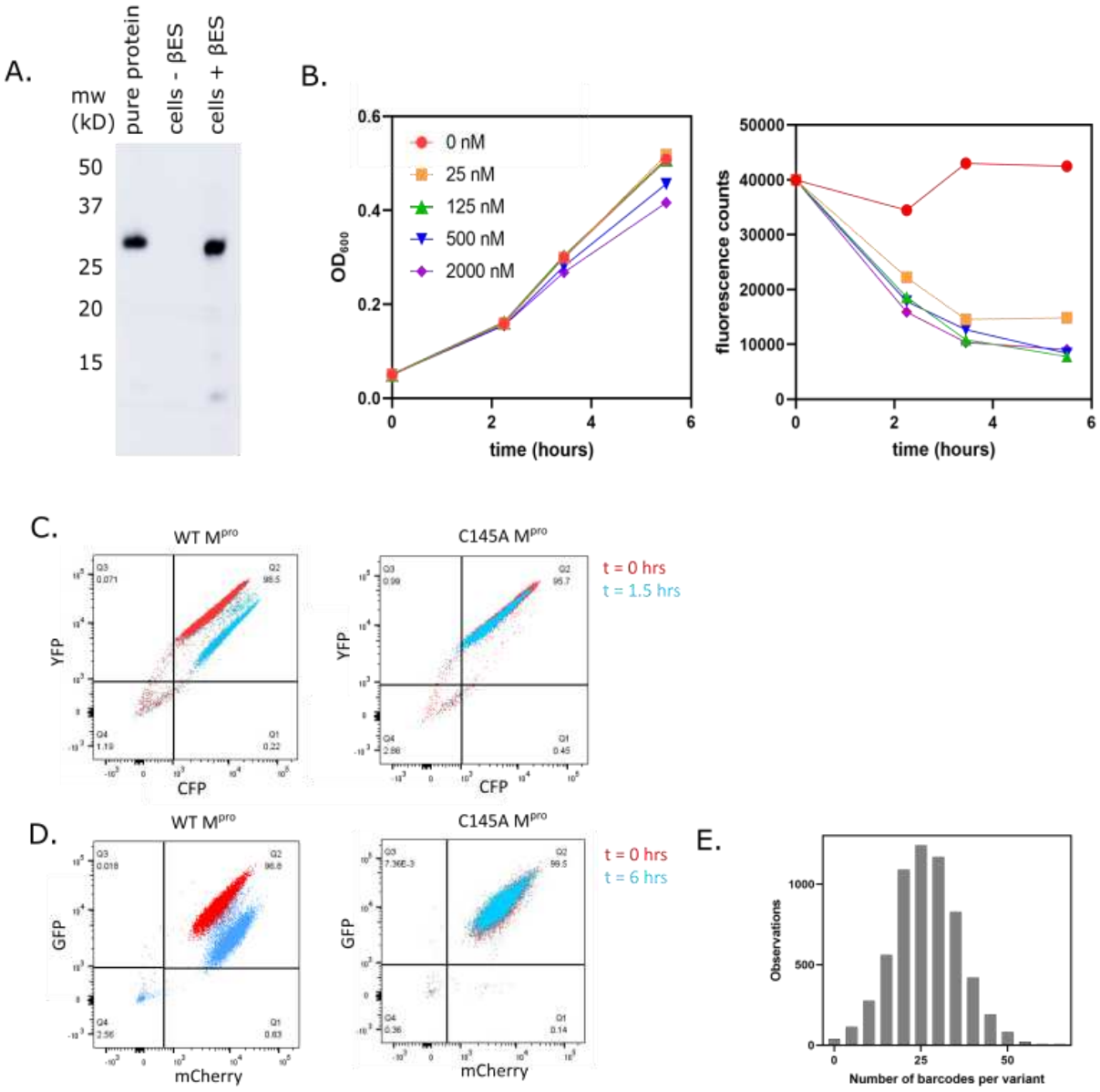


Figure S1. **M$^{pro}$ expression in cells harboring the LexA-UbM$^{pro}$ plasmid construct.** A. Yeast cells transformed with a plasmid expressing C145A Ub-M$^{pro}$-His$_6$ under the LexA promoter were grown to exponential phase followed by the addition of 2 µM β-estradiol to induce expression for 8 hours. M$^{pro}$ levels were monitored by Western blot with an anti-His$_6$ antibody and the correct size was measured against purified M$^{pro}$-His$_6$ protein (control). B. The plasmid expressing WT Ub-M$^{pro}$ under control of the LexA promoter was transformed into cells expressing the split transcription factor. Cells were grown to exponential phase followed by addition of the indicated concentration of β-estradiol. Cell density was monitored based on absorbance at 600 nm at the times indicated (left panel). At the same time points, cells were washed, diluted to equal cell number, and GFP fluorescence was monitored at 525 nm (right panel). C. FACS analysis of cells expressing the CFP-M$^{pro}$CS-YFP FRET pair and either WT Ub-M$^{pro}$ (left) or C145A Ub-M$^{pro}$ (right). Cell samples were collected before and after induction of M$^{pro}$ expression with 125 nM β-estradiol for 1.5 hours. D. FACS analysis of cells expressing the split transcription factor separated by the M$^{pro}$ cut-site and either WT Ub-M$^{pro}$ (left) or C145A Ub-M$^{pro}$

The final screen leverages the toxicity of $M^{pro}$ expression in yeast, which likely results from cleavage of essential yeast proteins by the protease (Alalam, Sigurdardottir et al. 2021). Increasing concentrations of β-estradiol correlates with a decrease in yeast growth rate that is dependent on the presence of catalytically-functional $M^{pro}$ (Figure 1c and S1b). At a high expression level, yeast growth rate becomes tightly coupled to $M^{pro}$ function and can be used as a readout of the function of the expressed $M^{pro}$ variant. While the endogenous yeast substrates are unknown, this assay is likely reporting on $M^{pro}$ cleavage of numerous cellular targets. Sampling of more than one cleavage site may better represent the physiologic role of $M^{pro}$, which has 11 viral and numerous host cleavage sites.

**Comprehensive deep mutational scanning of $M^{pro}$**

We integrated our three screens with a systematic mutational scanning approach to determine the impact of each single amino acid change in $M^{pro}$ on its function (Figure 1d). A comprehensive $M^{pro}$ single site variant library was purchased commercially (Twist Biosciences). Each position of $M^{pro}$ was mutated to all other 19 amino acids plus a stop codon, using the preferred yeast codon for each substitution. We transferred the library to a plasmid under the LexA promoter. To efficiently track each variant of the library using deep sequencing, we employed a barcoding strategy that allowed us to track mutations across the gene using a short sequence readout. We engineered the barcoded library so that each mutant was represented by 20-40 unique barcodes and used PacBio sequencing to associate barcodes with $M^{pro}$ mutations (Figure 1d). 96% of library variants were linked to 10 or greater barcodes (Figure S1e). As a control, the library was doped with a small amount of WT $M^{pro}$ linked to approximately 150 barcodes.

We transformed the plasmid library of $M^{pro}$ mutations into yeast strains harboring the respective reporter for each functional screen. The mutant libraries were amplified in the absence of selection and subsequently β-estradiol was added to induce $M^{pro}$ expression. For the fluorescent screens, the cells were incubated with β-estradiol at the concentration determined to limit $M^{pro}$ toxicity (125 nM) for the time required for WT $M^{pro}$ to achieve full reporter activity (1.5 hours for the FRET screen and 6 hours for the TF screen). Subsequently cells were separated by FACS into populations with either uncleaved or cleaved reporter proteins (See Figure 1a and 1b). For the growth screen, cells were incubated with a higher concentration of β-estradiol determined to slow yeast growth (2 μM) (Figure 1c and S1b). Populations of cells were collected at the 0- and 16-hour time points. For each cell population in each screen, plasmids encoding the mutated $M^{pro}$ library were recovered, and the barcoded region was sequenced using single end Illumina sequencing. For the TF and FRET screens, the functional score of each mutant was calculated as the fraction of the mutant in the cut population relative to its fraction in both populations. For the growth screen, the functional score was calculated as the fraction of the mutant at the 0-hour time point relative to the fraction in the 0-hour and 16-hour time points. We normalized the functional scores in all three screens to facilitate comparisons, setting

the score for the average WT $M^{pro}$ barcode as 1 and the average stop codon as 0 (See Table 1 for all functional scores).

To analyze the reproducibility of each screen, we performed biological replicates. For each biological replicate we separately transformed the library into yeast cells, and independently performed competition experiments and sequencing. Functional scores between replicates were strongly correlated ($R^2$> 0.98 for all three screens, Figure 2a) and we could clearly distinguish between functional scores for WT $M^{pro}$ and those containing stop codons (Figure 2b). There was a narrow distribution of functional scores for stop codons in all three screens across the $M^{pro}$ sequence except at the last seven positions (amino acids 300-306) (Figure 2c), supporting previous experiments showing that these residues are dispensable for $M^{pro}$ activity and the importance of residue Q299 for $M^{pro}$ function (Lin, Chou et al. 2008). We categorized functional scores as WT-like, intermediate, or null-like based on the distribution of WT barcodes and stop codons in each screen (Figure 2d). Heatmap representations of the functional scores determined in all three screens are shown in Figure 3.

**Comparison between three screens**

Comparing the average functional score at each position (a measure of mutational sensitivity) between the three screens shows a strong correlation (Figure 4a-c). The principal differences lie in the sensitivity of the screens to mutation, with the average defective mutation in the growth screen being more exaggerated than that in the fluorescent-based screens (Figure 4c). The scores in the growth screen are likely integrating cutting efficiency over a diverse set of cleavages sites which may contribute to this screen's increased sensitivity to mutation. Despite these differences, there are striking correlations in the mutational patterns of $M^{pro}$ across all three screens as can be visualized in the heatmap of average scores per position and when mapped to $M^{pro}$'s structure (Figure 4a and b). These similarities indicate that the three screens are reporting the same fundamental biophysical constraints of the protein.

Several lines of evidence indicate that the functional scores are biochemically and biologically relevant. First, we compared the scores to previously published studies of point mutations (Figure 4d and Table 2). For example, mutating the residues of the catalytic dyad, C145 and H41, inactivates the protease both in our screen and in *in vitro* biochemical assays as expected (Hegyi, Friebe et al. 2002). Additionally, *in vitro* assays have shown that residues at the dimer interface including S10, G11 and

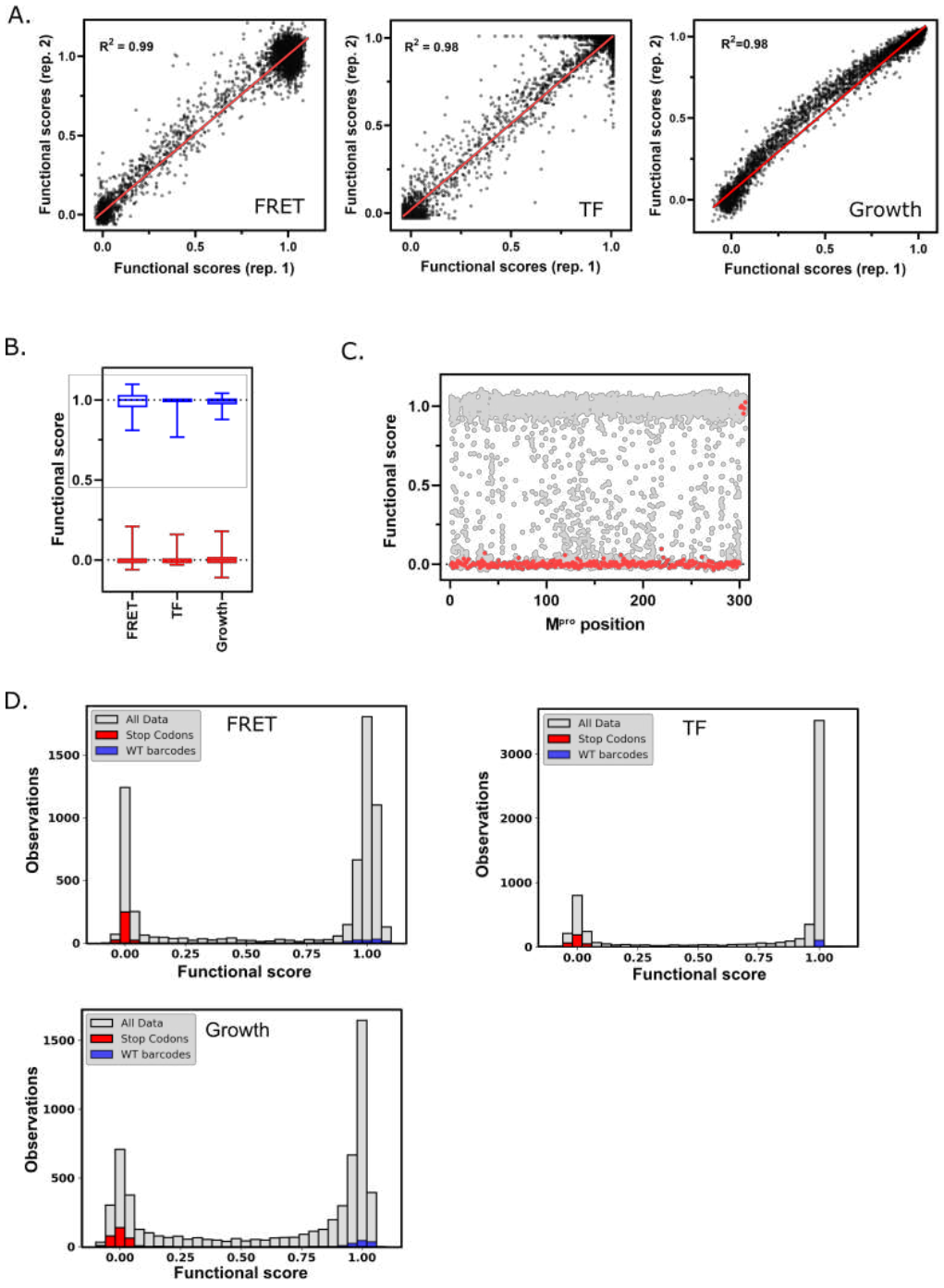


**Figure 2. M$^{pro}$ functional scores are reproducible, and variants can be clearly distinguished based on function**. A. Correlation between biological replicates of functional scores of all Mpro variants for each screen. Red line indicates best fit. B. Distribution of functional scores for stop codons (red) and WT barcodes (blue) in each screen. C. The functional scores for all variants (grey) and stop codons (red) at each position of M$^{pro}$ in the FRET screen. D. Distribution of all functional scores (grey) in each screen. Functional scores are categorized as WT-like, intermediate, or null based on the distribution of WT barcodes (blue) and stop codons (red) in each screen.

Figure 3a. FRET

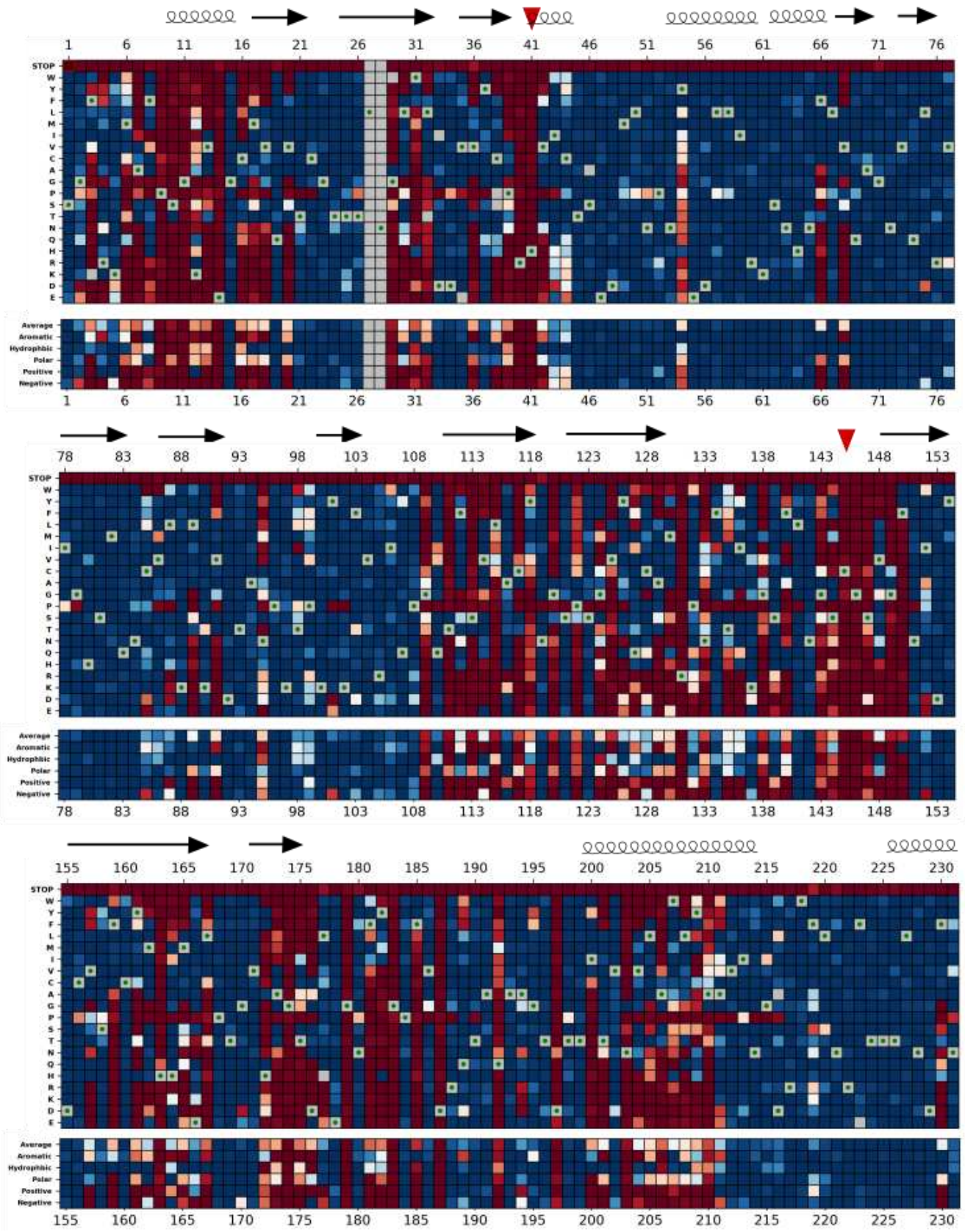

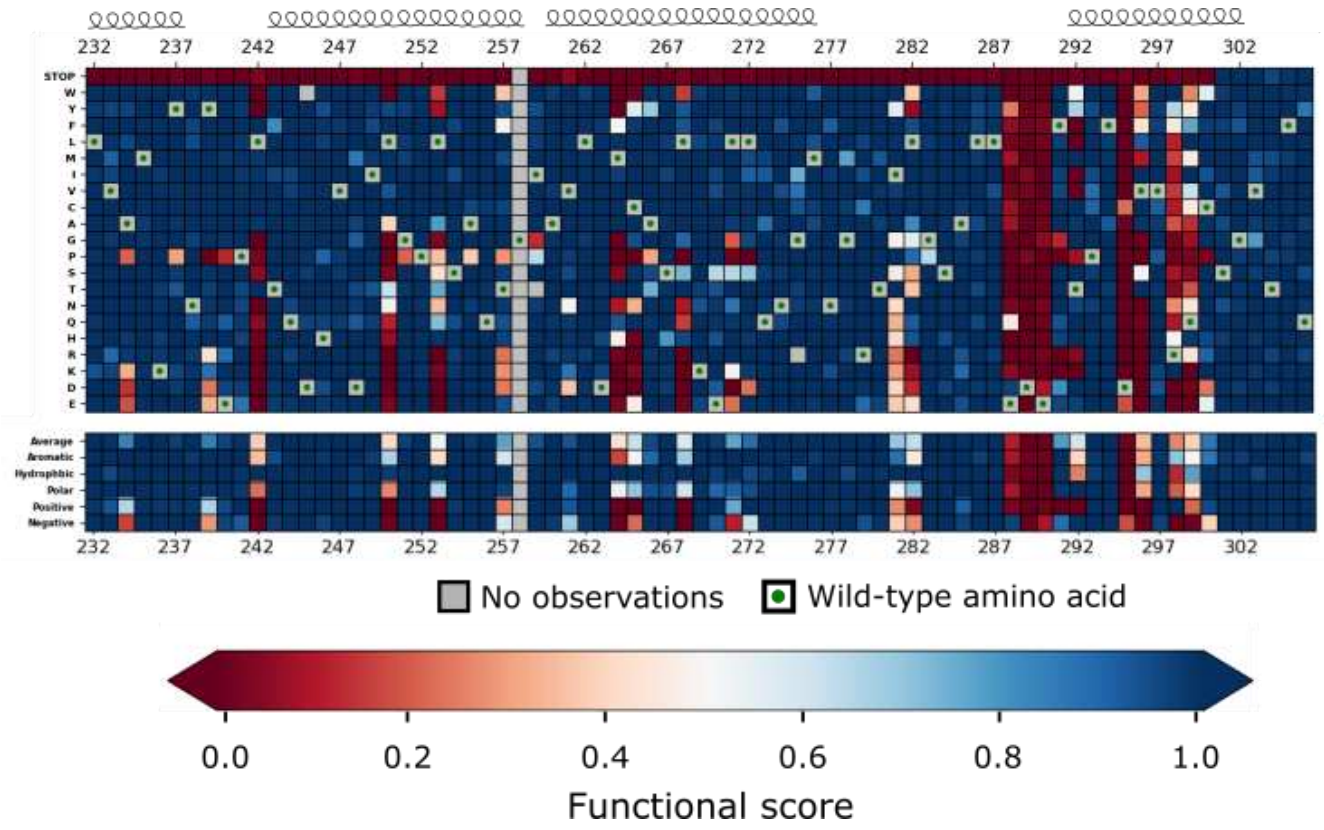

# Figure 3b - Transcription factor

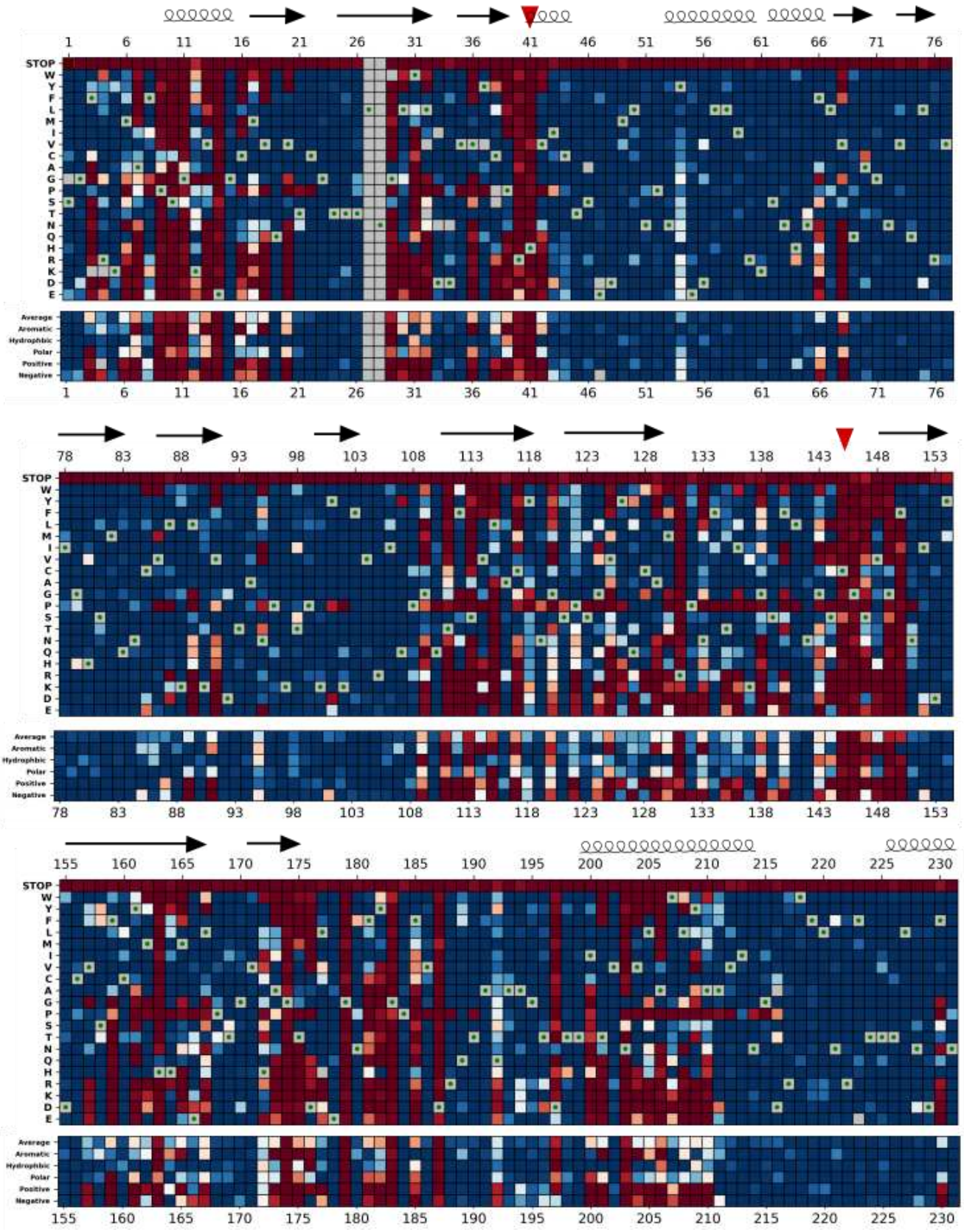

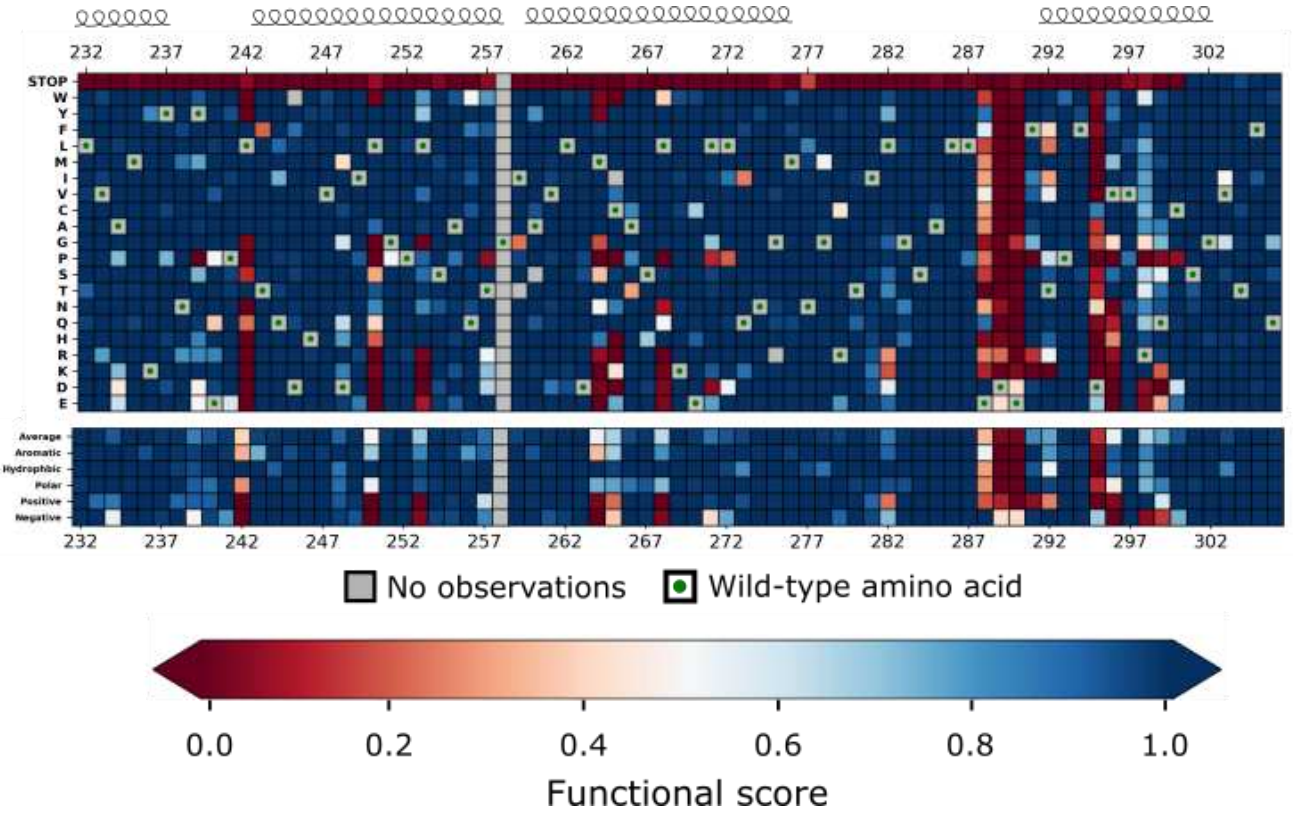

Figure 3c - Growth

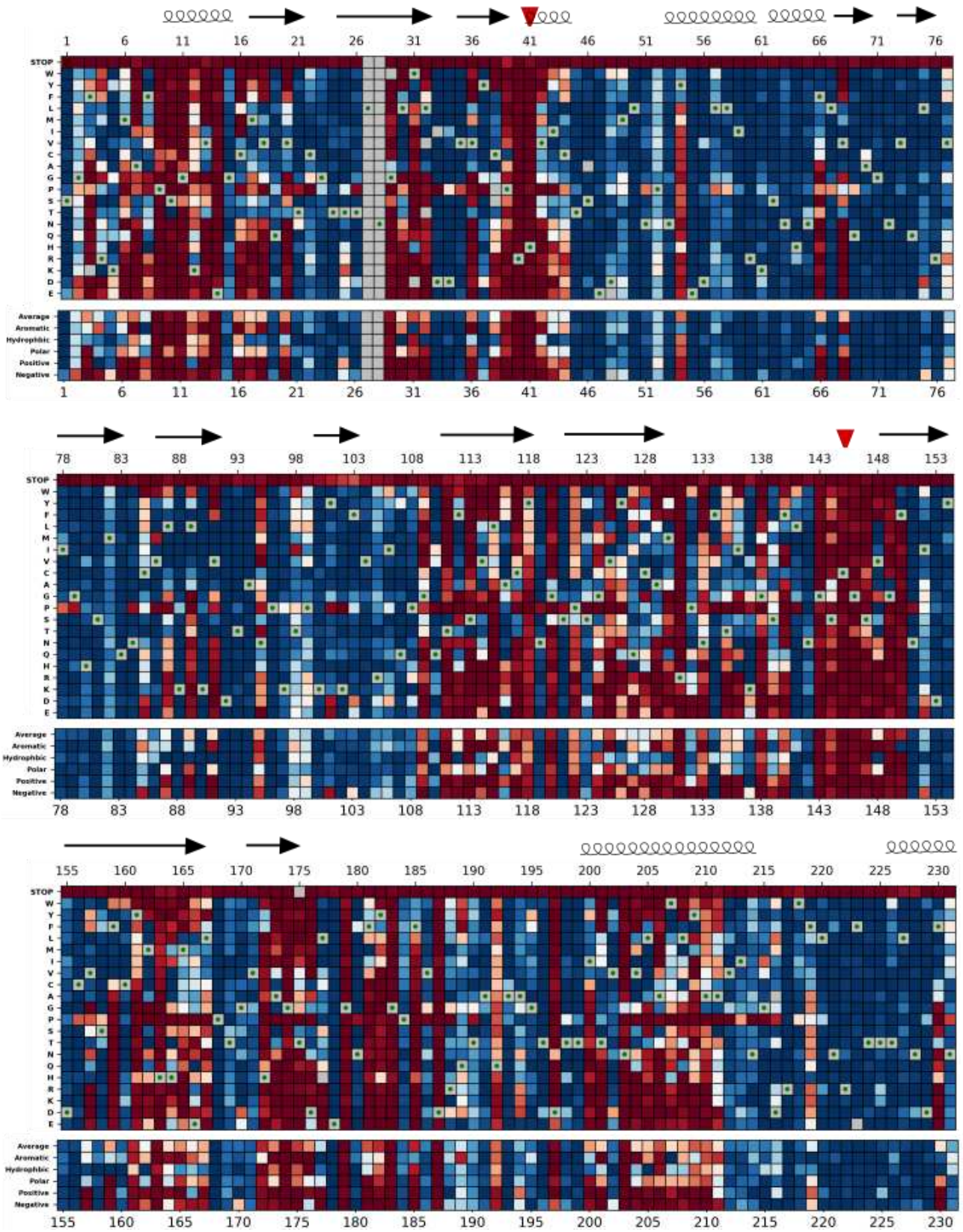

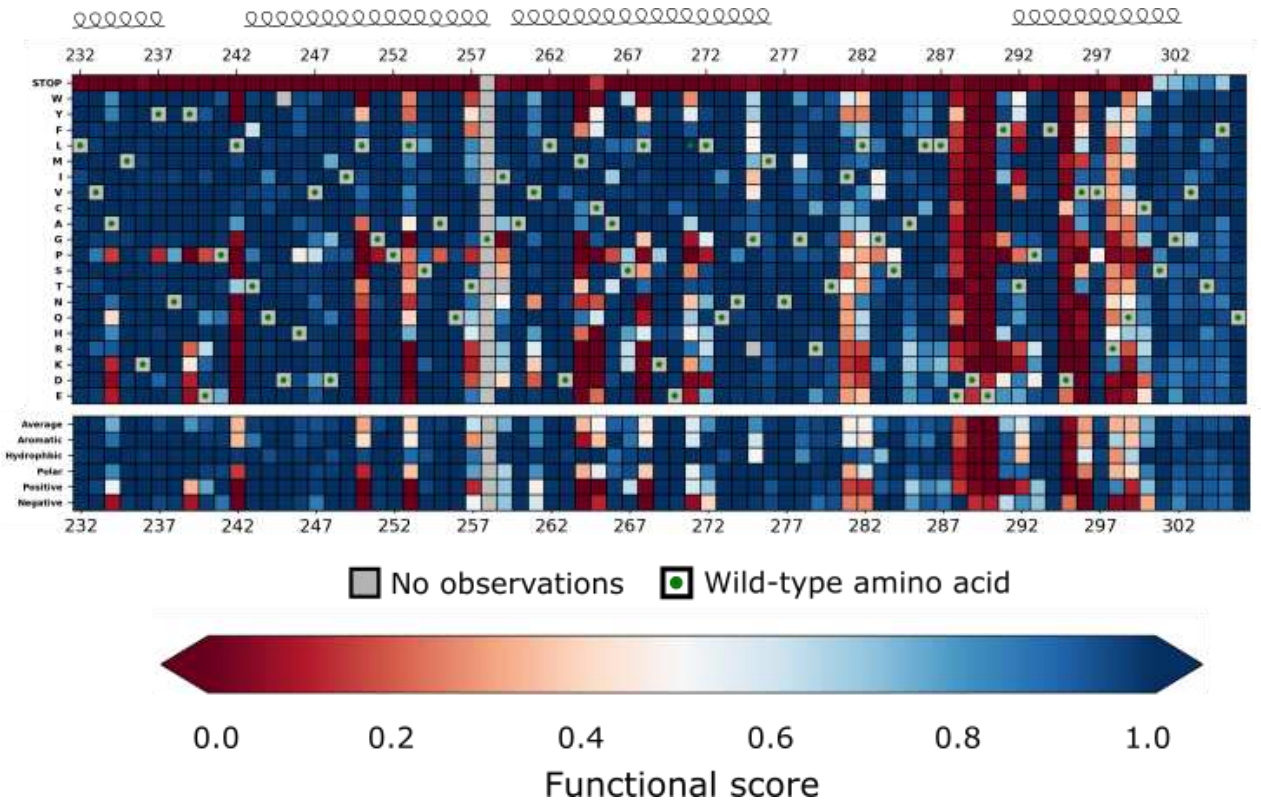


**Figure 3. Heatmap representation of the M$^{pro}$ functional scores measured in each screen**. A. Heatmap representation of scores from FRET screen. B. Heatmap representation of scores from transcription factor screen. C. Heatmap representation of scores from growth screen. Arrows represent positions that form beta sheets, coils represent α-helices, and red triangles indicate the catalytic dyad residues H41 and C145.

Figure 4.

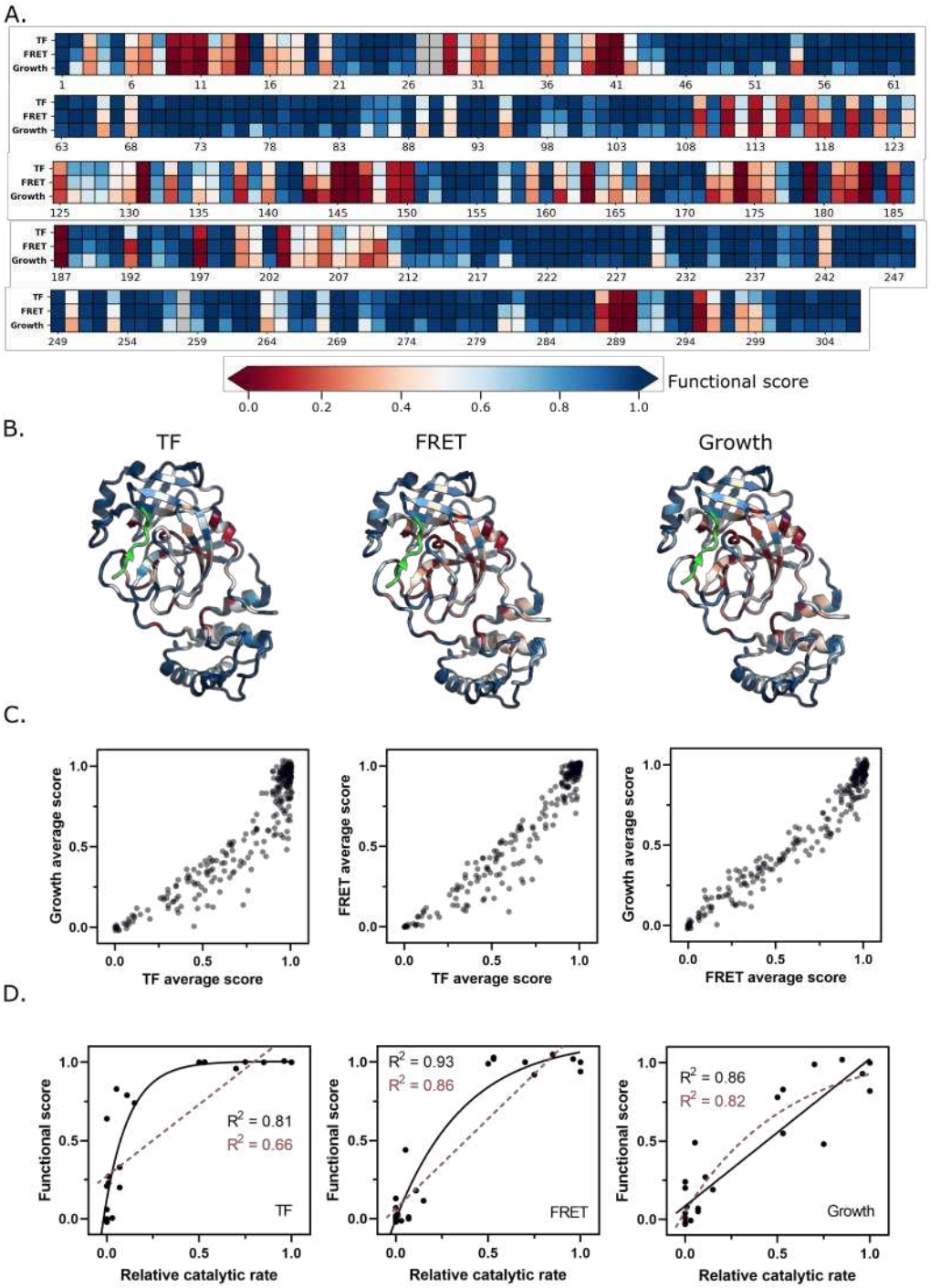


**Figure 4. Functional scores reflect fundamental biophysical constraints of M$^{pro}$**. A. Heatmap representation of the average functional score at each position (excluding stops) in each screen. B. The average functional score at each position mapped to M$^{pro}$ structure for each screen. The Nsp4/5 substrate peptide is shown in green (PDB 7T70). C. The average functional score at each position compared between the three screens. D. Comparison between relative catalytic rates measured independently in various studies and functional scores measured in each screen (see Table 2 for data). Each graph is fit with a non-linear and linear regression with the best of the two fits represented with a black solid line and the worst fit represented with a red dashed line. The non-linear regression is fit to the equation $Y = Ym-(Y0-Ym)e^{-kx}$.

**Table 2. Comparison of previously measured relative catalytic rates of individual mutations to functional scores**

| Mutation | $M^{pro}$ | Relative cat. rate | Functional score | | | PMID |
|---|---|---|---|---|---|---|
| | | | TF | FRET | Growth | |
| **R4A** | CoV-1 | 0.75 | 1.00 | 0.92 | 0.48 | 15554703 |
| **R4E** | CoV-1 | 0.01 | 0.23 | 0.02 | 0.08 | 16329994 |
| **K5A** | CoV-1 | 0.70 | 0.96 | 1.00 | 0.99 | 16329994 |
| **M6A** | CoV-1 | <0.01 | 0.64 | 0.07 | 0.20 | 16329994 |
| **P9T** | CoV-2 | 0.03 | 0.00 | -0.01 | 0.00 | 33208735 |
| **H41A** | CoV-2 | 0.00 | 0.00 | 0.02 | 0.01 | 34249864 |
| **H41D** | CoV-2 | 0.00 | 0.06 | -0.02 | -0.02 | 34249864 |
| **H41E** | CoV-2 | 0.00 | 0.00 | 0.01 | -0.03 | 34249864 |
| **P108S** | CoV-2 | 0.85 | 1.00 | 1.05 | 1.02 | Abe et al, 2021 |
| **S123A** | CoV-1 | 1.00 | 1.00 | 0.94 | 0.82 | 18275836 |
| **S123C** | CoV-1 | 1.00 | 1.00 | 1.03 | 1.00 | 18275836 |
| **S139A** | CoV-1 | 0.96 | 1.00 | 1.02 | 0.93 | 17154528 |
| **S144A** | CoV-1 | 0.53 | 1.00 | 1.02 | 0.55 | 17154528 |
| **C145A** | CoV-2 | 0.00 | -0.02 | 0.02 | -0.02 | 34249864 |
| **C145S** | CoV-2 | 0.00 | 0.21 | 0.00 | 0.04 | 34249864 |
| **S147A** | CoV-1 | 0.01 | 0.27 | 0.03 | 0.08 | 17154528 |
| **E166A** | CoV-1 | 0.50 | 1.00 | 0.99 | 0.78 | 20371333 |
| **E290A** | CoV-1 | 0.00 | 0.00 | 0.02 | -0.03 | 15554703 |
| **R298A** | CoV-1 | 0.11 | 0.79 | 0.18 | 0.27 | 18275836 |
| **R298K** | CoV-1 | 0.53 | 1.00 | 1.03 | 0.83 | 18275836 |
| **R298L** | CoV-1 | 0.15 | 0.74 | 0.12 | 0.19 | 18275836 |
| **Q299A** | CoV-1 | 0.02 | 0.84 | 0.13 | 0.24 | 18275836 |
| **Q299E** | CoV-1 | 0.07 | 0.33 | 0.01 | 0.07 | 18275836 |
| **Q299K** | CoV-1 | 0.07 | 0.20 | 0.00 | 0.05 | 18275836 |
| **Q299N** | CoV-1 | 0.05 | 0.93 | 0.44 | 0.49 | 18275836 |

E14 are essential for SARS-CoV-1 $M^{pro}$ dimerization and function (Chen, Zhang et al. 2008). Mutations at these residues are also deleterious to $M^{pro}$ function in our screen. Because of the high sequence and functional similarities between SARS-CoV-1 and CoV-2 $M^{pro}$, we expect that the majority of the mutational analyses performed previously on SARS-CoV-1 $M^{pro}$ will be valid for SARS-CoV-2 $M^{pro}$. We observe an apparent non-linear relationship between the functional scores measured in both the FRET and TF screens and the relative catalytic activity of mutants measured independently for $M^{pro}$ *in vitro* in various studies ($R^2$ = 0.81 for non-linear fit to TF screen and $R^2$ = 0.93 for non-linear fit to FRET screen) (Figure 4d). Compared to the fluorescent screens, there is a stronger linear relationship ($R^2$ = 0.86) between the scores measured in our growth screen and the catalytic efficiencies of the individual mutants. The growth screen appears to more fully capture the dynamic range of mutations with slight functional defects that tend to appear WT-like in the FRET and TF screens. For the remainder of this

paper, we will report the functional scores collected from both the FRET and growth screens. The advantage of the functional scores for each mutant from the FRET screen is that they report direct cleavage of a defined substrate, with the drawback being that they exhibit less sensitivity to mutation. The advantage of the growth screen is that the functional scores show a more linear relationship with catalytic rate while the drawback is that the screen reports cleavage of undefined substrates. Because of the correlation between all three screens, similar overall biophysical conclusions are supported by each screen.

**Functional characterization of natural M$^{pro}$ variants**

To further assess the scores from our screen, we examined the functional scores of the M$^{pro}$ variants observed in clinical samples. Because M$^{pro}$ is essential for viral replication, deleterious mutations should be purged from the circulating population. The CoV-Glue-Viz database archives all mutations observed in the GISAID hCoV-19 sequences sampled from the ongoing COVID-19 pandemic (Singer, Gifford et al. 2020). We compared the frequency at which the clinical variants of the M$^{pro}$ gene (ORF1ab/nsp5A-B) have been observed to their functional scores and found that the most abundant clinical variants are highly functional in our assays (Figure 5a). However, lower frequency variants in clinical samples were found to have a wide range of M$^{pro}$ function. Surprisingly, M$^{pro}$ sequences among the clinical samples include premature stop codons that have been observed up to 100 times (out of over 5 million total isolates to date) (Figure 5a). Because M$^{pro}$ function is required for viral fitness, we assume that the frequency of stop codons observed in the data is an indication of sequencing error in the clinical samples. Accounting for this sequencing error, we examined the functional score of the 290 nonsynonymous mutations in the M$^{pro}$ gene that have been observed more than 100 times. The vast majority of these clinical variants exhibit WT-like function with only nine having a score below that of the WT distribution (see Figures 5a-c). This observed enrichment for variants with WT-like function in the circulating SARS-CoV-2 virus indicates that M$^{pro}$ is undergoing strong purifying selection in the human population.

Figure 5

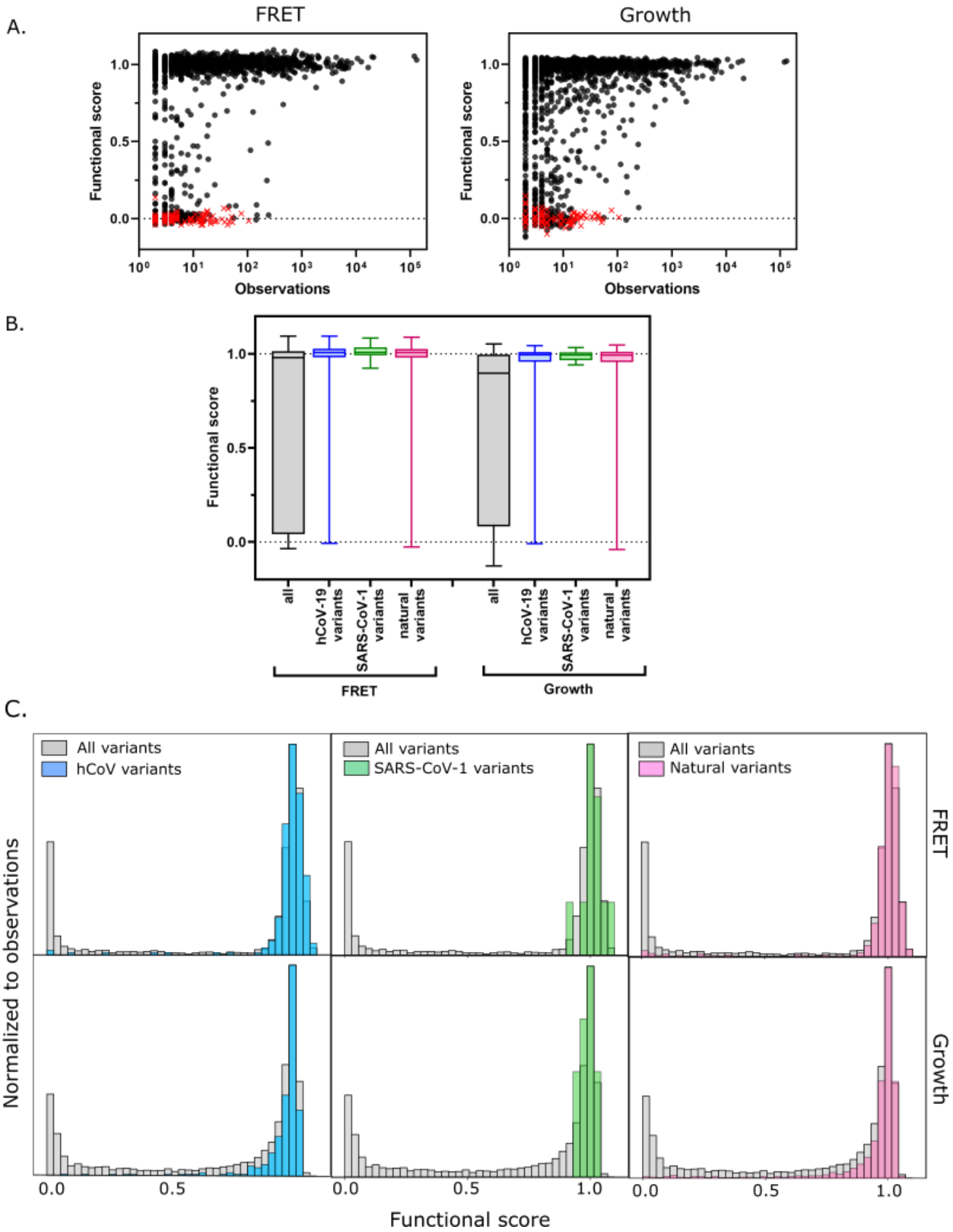

**Figure 5. Functional scores indicate that natural amino acid variants of M$^{pro}$ are generally fit.** A. Comparison of functional scores in the FRET screen (left panel) and growth screen (right panel) to the number of observations among clinical samples. All missense mutations excluding stops are indicated with black circles and stop codons are indicated with red x's. B. The distribution of functional scores of all variants in the FRET and growth screens compared to the observed clinically-relevant M$^{pro}$ variants (hCoV-19 variants, blue), 12 amino acid differences between SARS-CoV-2 and SARS-CoV-1 (green), and the different amino acids in a broad sample of M$^{pro}$ SARS-CoV-2 homologs (natural variants, pink). Distributions are significantly different as measured by a two-sample Kolmogorov-Smirnov (KS) (All FRET vs. hCoV-19 variants: N = 6044, 289, p<0.0001, D = 0.3258; All FRET vs. SARS-CoV-1 variants: N=6044, 12, p=0.0398, D=0.4223; All FRET vs. natural variants: N = 6044, 1205, p<0.0001, D = 0.2984; All Growth vs. hCoV-19 variants: N = 6044, 289, p<0.0001, D = 0.3938; All growth vs. SARS-CoV-1 variants: N=6044, 12, p=0.0024, D=0.5533; All growth vs. natural variants: N=6044,1205, p<0.0001, D = 0.3462) C. Histogram of functional scores of all variants (grey) compared to that of hCoV-19 variants (blue), SARS-CoV-1 variants (green), and natural variants (pink).

Additionally, we examined the experimental function of M$^{pro}$ mutations compared with the diversity of M$^{pro}$ in viruses related to SARS-CoV-2. There is a 96% sequence identity between the SARS-CoV-2 and SARS-CoV-1 M$^{pro}$ proteases, with only 12 amino acid differences. In our study, all of the amino acid differences in SARS-CoV-1 M$^{pro}$ are WT-like in SARS-CoV-2, underscoring the credibility of the functional scores and indicating a lack of strong epistasis between the 12 substitutions (Figure 5b). We went on to analyze the diversity in 852 sequences across a set of M$^{pro}$ homologs from genetically diverse coronaviruses. We identified 1207 amino acid changes located at 263 positions of M$^{pro}$ and examined the functional score of these variants in our data. Here again, we saw enrichment towards functional M$^{pro}$ variants with only 6% (77 out of 1207) natural variants having functional scores in the FRET screen below the WT range (Figure 5b and 5c). Further analysis of these deleterious variants should provide insight into the role epistasis played in the historical evolution of M$^{pro}$, and these insights may have utility in the generation of future pan-coronavirus inhibitors.

## Structural distribution of mutationally-sensitive M$^{pro}$ positions

Invariant sites that are essential to M$^{pro}$ function are promising targets for designing inhibitors. 24 positions of M$^{pro}$ exhibited low mutation tolerance, defined as 17 or more substitutions with null-like function: P9, S10, G11, E14, R40, H41, T111, S113, R131, C145, G146, S147, G149, F150, H163, G174, G179, G183, D187, D197, N203, D289, E290, and D295 (Figure 6a). Only four of these mutation-sensitive residues contact the substrate: H41 and C145 (the catalytic residues), as well as H163, and D187. H163 interacts with the invariable P1 Gln of the substrate and D187 forms a hydrogen bond with a catalytic water and a salt bridge with R40. A large body of work has previously shown that dimerization is indispensable to M$^{pro}$ function (Chou, Chang et al. 2004, Hsu, Chang et al. 2005, Chen, Zhang et al. 2008, Cheng, Chang et al. 2010). Our study also supports the critical functional role of

Figure 6

A.

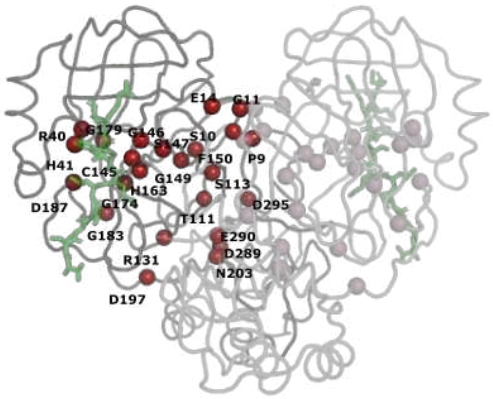


B.

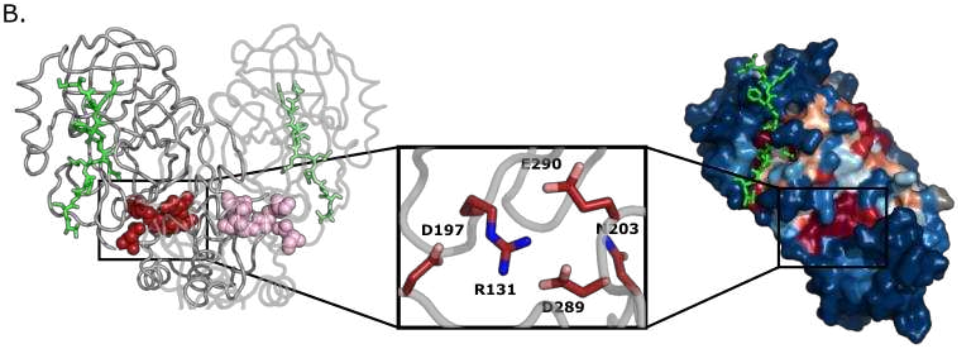


C.

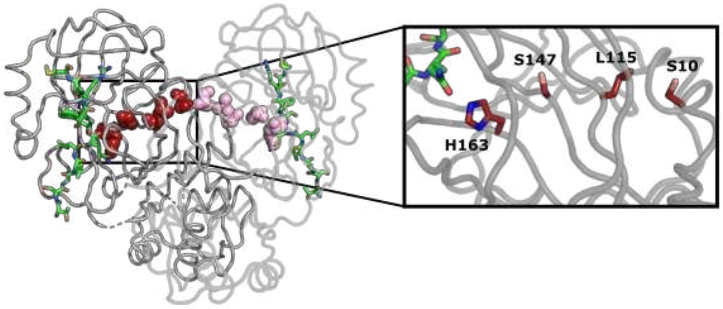


D.

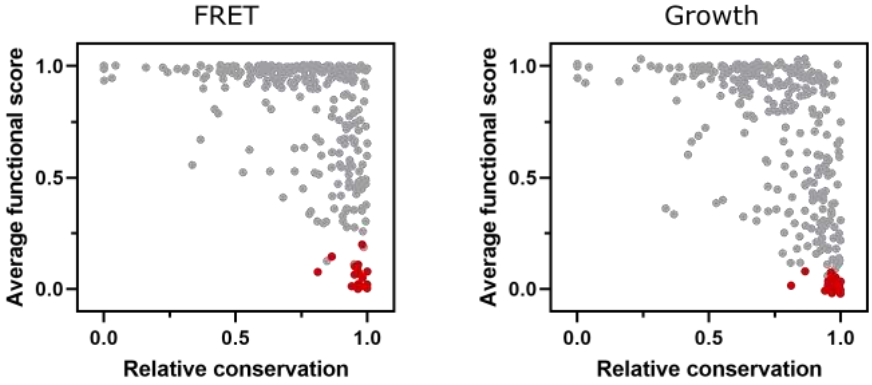

**Figure 6. Structural distribution of M$^{pro}$ positions that are intolerant to mutation**. A. M$^{pro}$ positions that are intolerant of mutations with 17 or more substitutions having null-like function are represented by red spheres on chain A (shown in grey) and pink spheres on chain B (shown in white). The Nsp4/5 substrate peptide is shown in green (PDB 7T70). B. Representation of a cluster of the mutation-intolerant positions (red spheres) at a site distal to the active site. C. A cluster of mutation-intolerant residues (red spheres) appear to be part of an allosteric communication network between the active site and the dimerization interface. D. Comparison of the average functional score of each position to conservation observed in a broad sample of SARS-CoV-2 M$^{pro}$ homologs. The 24 mutation-intolerant positions shown as red spheres in part A are highlighted in red. Positions exhibiting the strongest evolutionary conservation exhibit a broad range of experimental sensitivity to mutation while the most evolutionary variable positions are experimentally tolerant to mutations.

dimerization as we see prevalent mutation-sensitivity in residues at the dimer interface, including P9, S10, G11, E14, and E290, each of which cannot be altered without complete loss of function.

Outside of these well-studied critical M$^{pro}$ sites, there are additional clusters of mutation-intolerant residues. R131, D197, N203, D289 and E290 lie at the interface of Domain II and Domain III sandwiched between dimers and make up part of a surface identified by structural modeling as a possible distal drug binding pocket (Bhat, Chitara et al. 2021, Weng, Naik et al. 2021) (Figure 6b). Within this cluster, a dynamic salt bridge is formed between R131 located on the loop of Domain II connecting β10-11 of the catalytic pocket, and D289 in the α-helical Domain III that has been reported to contribute to the flexibility and structural plasticity of M$^{pro}$ (Bhat, Chitara et al. 2021). The location of these residues at the interface of the two domains and the dimer interface, combined with the fact that they are critical to M$^{pro}$ function suggests that they are part of an allosteric communication network. Our studies clearly indicate the critical function played by this network of residues providing motivation for further examination of their potential as a mutation-resistant target for inhibitor design.

A second cluster of mutation-intolerant residues appear to be part of an allosteric communication network between the active site and the dimerization interface. Prior studies of individual mutations also suggest allosteric connections between the dimerization and active sites. Mutations at both E166 (Cheng, Chang et al. 2010) and S147 (Barrila, Bacha et al. 2006) were found to disrupt dimerization. Both positions E166 and S147 are located distal to the dimerization site, suggesting that the properties of these two sites are interdependent. Our results show that there is a physically-interacting chain of mutation-sensitive residues that bridge from the active site to the dimerization site (Figure 6c). This bridge is composed of H163 that directly contacts the P1 Gln of substrate, S147, L115 and S10 at the dimer interface. Each of these dimer-to-active site bridging residues are critical to M$^{pro}$ function and are strongly conserved among M$^{pro}$ homologs. Based on these observations, we suggest that the

physical interactions between H163, S147, L115, and S10 mediate critical communication between the active sites of both subunits in the $M^{pro}$ dimer.

All 24 of the identified mutation-intolerant residues are highly conserved among SARS-CoV-2 $M^{pro}$ homologs (Figure 6d). While functional hot spots accurately predict evolutionary conservation, conservation does not accurately predict functional hot spots. There are many residues in $M^{pro}$ that are strongly conserved, but that can be mutated without strong impacts on function. This pattern has been widely observed for other proteins (Hietpas, Jensen et al. 2011, Melamed, Young et al. 2013, Roscoe, Thayer et al. 2013, Starita, Pruneda et al. 2013, Mishra, Flynn et al. 2016). While many features distinguish natural evolution and experimental studies of fitness (Boucher, Bolon et al. 2019) one of the outstanding differences is the strength of selection. While functional hot spots can be defined by strong impacts on function that are experimentally measurable, small fitness changes that may be too small for experimental resolution can drive selection in natural evolution due to large population sizes and timescales (Ohta 1973). Our functional screen captures the mutations that are critical to catalytic function while evolutionary conservation depicts a wide range of mutations including those that make more nuanced contributions to function.

**Functional variability at key substrate and inhibitor-contact positions**

$M^{pro}$ function is essential for SARS-CoV-2 replication, making it a key drug target. To help further guide inhibitor design, we assessed the mutations that are compatible with function and that should be readily available to the evolution of drug resistance. We focused these analyses on the active site, which is the target binding site for most inhibitors that have been generated against $M^{pro}$ (Cho, Rosa et al. 2021). In Figure 7a, we highlight all the $M^{pro}$ residues that contact the Nsp4/5 peptide, either through hydrogen bonds or van der Waals interactions (Shaqra, Zvornicanin et al. 2022). In our functional screens, we found dramatic variability in mutational sensitivity at these substrate-contact positions. For example, residues G143, H163, D187 and Q192 were extremely sensitive to mutation while residues M49, N142, E166 and Q189 were highly tolerant. Despite the diverse sequence variation amongst $M^{pro}$'s substrates, they occupy a conserved volume in the active site, known as the substrate envelope, and the interactions between $M^{pro}$'s residues and all of its substrates are highly conserved (Shaqra, Zvornicanin et al. 2022) indicating that our mutation results from the Nsp4/5 cut-site will likely translate to other cut-sites.

Figure 7

A.

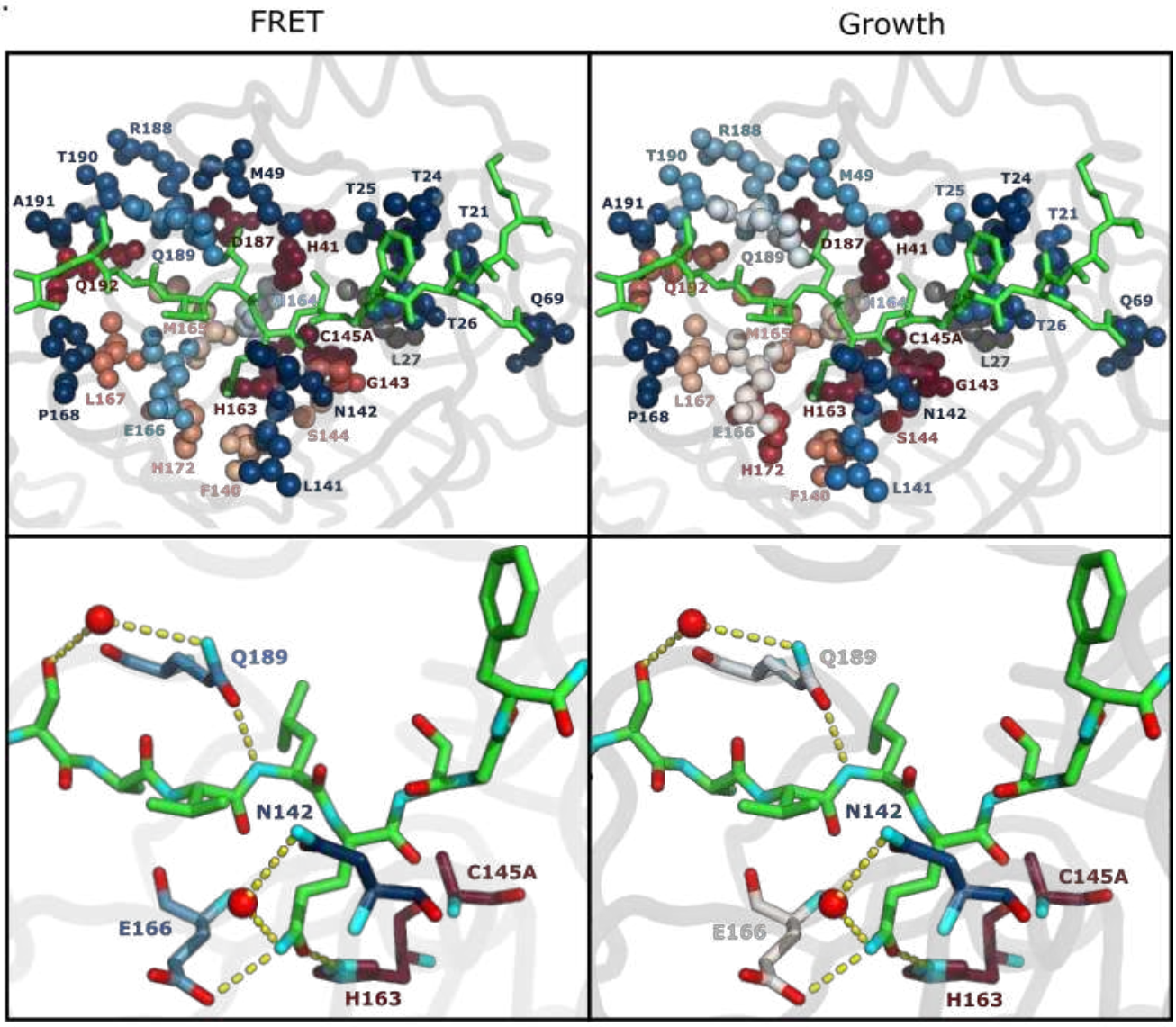

B.

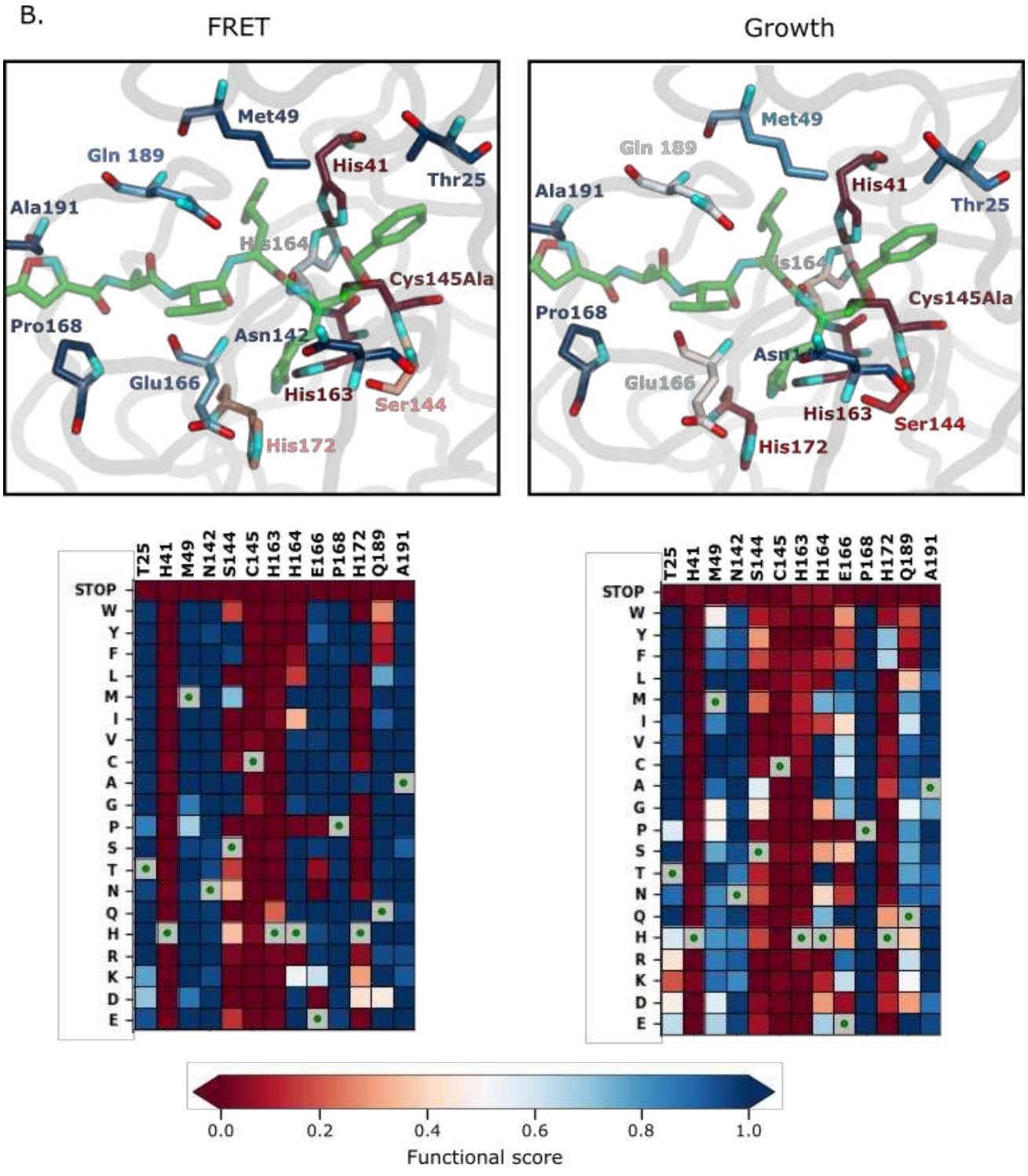

C.

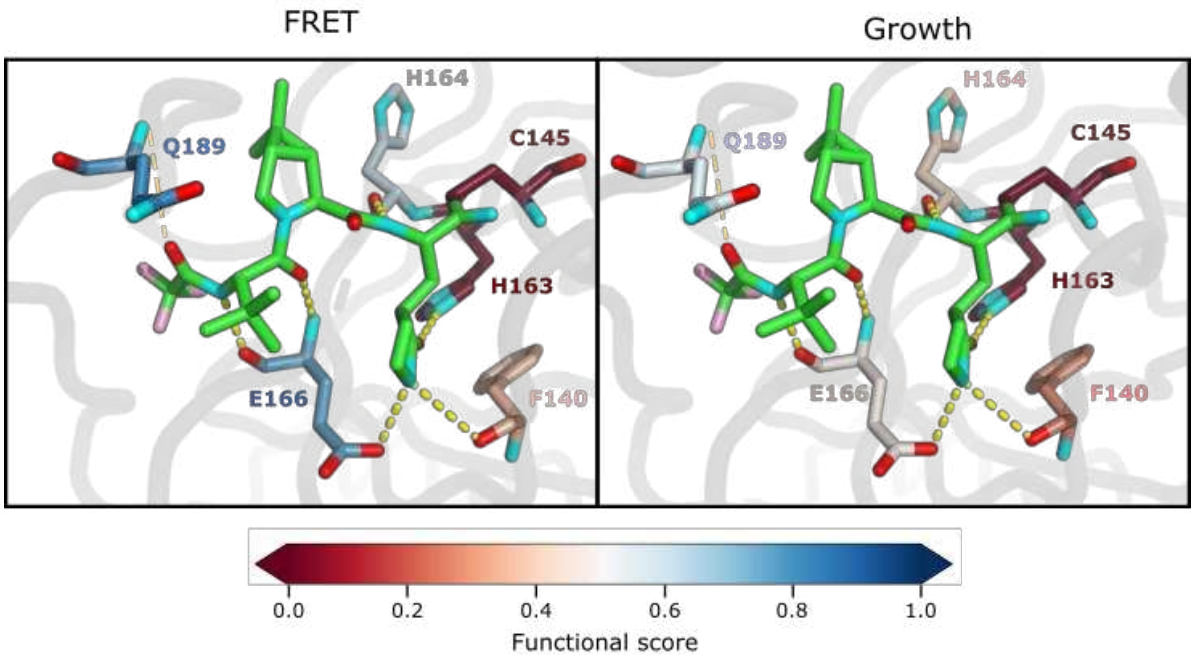


| Mutation | ΔΔG | Codon change | FRET score | Growth score |
|---|---|---|---|---|
| **Q189E** | 1.11 | CAA -> GAA | 1.04 | 1.0 |
| **E166A** | 1.0 | GAA -> GCA | 1.0 | 0.88 |
| **E166Q** | 1.0 | GAA -> CAA | 1.0 | 0.96 |

**Figure 7. Substrate and inhibitor binding sites are variably sensitive to mutation**. A. Top panel: All $M^{pro}$ positions that contact the Nsp4/5 substrate peptide are represented in spheres and colored by their average FRET functional score (left panel) and growth functional score (right panel) (PDB 7T70). The Nsp4/5 peptide is shown in green. Bottom panel: $M^{pro}$ positions that form hydrogen bonds with the Nsp4/5 substrate are shown in sticks and colored by their average FRET functional score (left panel) and growth functional score (right panel) (PDB 7T70). Oxygens are shown in red and nitrogens in cyan. Water molecules are represented as red spheres and hydrogen bonds as yellow dashed lines. B. Top panel: $M^{pro}$ positions shown to contact over 185 inhibitors in crystal structures (Cho, Rosa et al. 2021) are shown in sticks and are colored by their average FRET functional score (left panel) and average growth functional score (right panel). Shown is a representative structure of $M^{pro}$ bound to the N3 inhibitor (PDB 6LU7) (Jin, Du et al. 2020). The N3 inhibitor is shown in green, oxygens in red, and nitrogens in cyan. Bottom panel: Heatmap representation of functional scores for the FRET screen (left panel) and the growth screen (right panel) at key inhibitor-contact positions as illustrated above. C. $M^{pro}$ positions that form hydrogen bonds with the Pfizer inhibitor, PF-07321332, are represented by sticks and colored by their average FRET functional score (left panel) or growth functional score (right panel) (PDB 7VH8) (Owen, Allerton et al. 2021, Zhao, Fang et al. 2021). PF-07321332 is shown in green, oxygens in red, nitrogens in cyan. Hydrogen bonds less than 4 Å are represented with thick yellow dashed lines and greater than 4 Å with a thin yellow dashed line. The table below lists the mutations with highest potential for being resistant against PF-07321332.

Even among residues whose side chains make direct hydrogen bonds with substrates are positions that are surprisingly tolerant to mutation, namely N142, E166 and Q189. N142 forms distinct hydrogen bonds with Nsp4/5 and Nsp8/9, which has been proposed as a mechanism of $M^{pro}$ substrate recognition (MacDonald, Frey et al. 2021). Q189 is in a flexible loop that closes over the substrates, allowing accommodation of diverse cut-sites (Shaqra, Zvornicanin et al. 2022). In our screens, we find that these proposed substrate-recognition positions are very tolerant to mutation (Figure 7a) and have high potential for developing inhibitor resistance. Our results indicate that mutations at N142, E166 and Q189 are compatible with function and are readily available to the evolution of drug resistance.

A recent study comprehensively examined 233 X-ray crystal structures of SARS-CoV-2 $M^{pro}$ in complex with a wide range of inhibitors (Cho, Rosa et al. 2021). In 185 of these 233 structures, inhibitors lie in the same binding pocket in the active site, primarily contacting $M^{pro}$ positions T25, H41, M49, N142, S144, C145, H163, H164, E166, P168, H172, Q189 and A191. We therefore went on to determine the mutations at these key inhibitor binding residues that are compatible with $M^{pro}$ function and should likely be available to resistance evolution. Figure 7b illustrates a representative structure of $M^{pro}$ bound to the N3 inhibitor with the average mutational sensitivity of each position mapped to the structure by color (Jin, Du et al. 2020). In addition, a heatmap is shown detailing the mutations at these positions that are compatible with function. Of note, residues N142, E166, and Q189 form direct hydrogen bonds with many $M^{pro}$ inhibitors and most mutations at these positions result in a functional protease. Additionally, T25, M49, M164, P168 and A191 form van der Waals interactions with a variety of inhibitors suggesting that mutations at these positions could disrupt inhibitor interactions while maintaining $M^{pro}$ function. In contrast, positions H41, S144, C145, H163 and H172 are highly sensitive in our screen, as well as strongly conserved in nature, and therefore would be ideal contact positions for inhibitors with reduced likelihood of evolving $M^{pro}$ resistance.

Pfizer has developed the first FDA-authorized $M^{pro}$ inhibitor, PF-07321332 (Owen, Allerton et al. 2021). We examined the structure of $M^{pro}$ bound to PF-07321332 to identify positions with the potential to evolve resistance against this drug (Figure 7c) (Zhao, Fang et al. 2021). Evolutionarily-accessible resistance mutations are single base change mutations that would disrupt inhibitor binding while maintaining WT-like substrate recognition and cleavage. We identified all mutations of $M^{pro}$ that have WT-like function in both the FRET and growth screens, would lead to a predicted decrease in inhibitor binding energy upon mutation of greater than 1 kcal/mol, and are accessible with a single nucleotide base change. These criteria led to the identification of three mutations, Q189E, E166A and E166Q with potential resistance against PF-07321332. These three positions are at sites where the inhibitor protrudes out of the defined substrate envelope, providing further evidence that these residues may evolve inhibitor resistance while maintaining substrate recognition (Shaqra, Zvornicanin et al. 2022). Of note, Q189E is a natural variant in both the avian infectious bronchitis virus (IBV) and the swine coronavirus, HKU15 CoV, widely detected in pigs in Asia and North America and of pandemic concern

due to its ability to replicate in human cells (Edwards, Yount et al. 2020). PF-07321332 may have reduced efficacy against these concerning homologs due to its decreased interactions with Q189E $M^{pro}$.

In addition to the impacts on side-chain properties, mutations in $M^{pro}$ may also impact resistance through changes in main-chain conformation and dynamics, particularly in loops. In-depth structural analyses will be important to extensively assess the potential impacts of mutations on resistance through these mechanisms. Of note, mutations at N142 appears of particular interest for further investigation of conformational changes that may impact resistance evolution. N142 is mutation tolerant and located in a loop over the P1 position of the substrate. The lactam ring on PF-07321332 protrudes outside of the substrate envelope at this location (Shaqra, Zvornicanin et al. 2022). Mutations at position 142 should be readily available to $M^{pro}$ evolution and appear likely to influence loop conformation at a site where PF-07321332 extends beyond the substrate envelope. Together these observations suggest that N142 warrants further attention as a potential contributor to drug resistance.

## Discussion

During the SARS-CoV-2 pandemic, intensive efforts have been launched to rapidly develop vaccines and anti-viral drugs to improve human health. In this study, we provide comprehensive functional information on a promising therapeutic target, $M^{pro}$, with the hopes that these results will be useful in the design of more effective and long-lasting anti-SARS-CoV-2 drugs. We built three yeast screens to measure the functional effects of all individual amino acid changes in $M^{pro}$. The resulting fitness landscapes provide information on residues to both target and avoid in the drug design process. In the active site, the primary current target of $M^{pro}$ inhibitors, our results indicate both mutation-sensitive positions that provide ideal anchors for inhibitors, and mutation-tolerant positions to avoid. Among the positions to avoid, Q189 is noteworthy because it forms hydrogen bonds directly with substrates (MacDonald, Frey et al. 2021, Shaqra, Zvornicanin et al. 2022), contacts promising $M^{pro}$ drugs such as PF-07321332 (Cho, Rosa et al. 2021, Owen, Allerton et al. 2021, Zhao, Fang et al. 2021), is a natural variant in coronaviruses of future pandemic concern, and is surprisingly tolerant of mutations in our screen.

We found that the functional scores measured from all three distinct screens were highly correlated, that they identified known critical $M^{pro}$ residues, and that clinical variants were overwhelmingly functional, indicating that the scores successfully capture key biochemical and functional properties of $M^{pro}$. However, there are a couple of caveats that should be kept in mind when utilizing these data sets. For example, we do not fully understand how $M^{pro}$'s biochemical function relates to viral fitness. Having some $M^{pro}$ function is essential to the virus, so mutations that destroy $M^{pro}$ function will form non-functional viruses. Function-fitness relationships tend to be non-linear (Heinrich and Rapoport

1974, Kacser and Fell 1995, Jiang, Mishra et al. 2013) and it may be likely that $M^{pro}$ function must be decreased by a large amount in order to cause measurable changes in viral replication efficiency. This relationship between $M^{pro}$ function and SARS-CoV-2 fitness would need to be determined in order to translate our functional scores to fitness scores. Additionally, our TF and FRET screens quantify cleavage at one defined site (Nsp4/5) and it may be important to analyze all sites in order to fully understand the selection pressures acting on $M^{pro}$. Another important caveat is that our fitness landscape captures single amino acid changes and therefore does not provide information on the potential interdependence or epistasis between double and higher order mutations. Information regarding epistasis will be important for accurately predicting the impacts of multiple mutations on fitness. Despite these caveats, the similarity in fitness landscapes for the TF and FRET screens with the yeast growth screen suggests that all three capture fundamental and general aspects of $M^{pro}$ selection. In addition, the high function of almost all naturally occurring substitutions in the diversity of natural $M^{pro}$ sequences indicates that estimates of fitness effects in different genetic backgrounds can be made based on our results.

We believe that our results will be a useful guide for the continuing intense efforts to develop drugs that target $M^{pro}$ and the interpretation of future $M^{pro}$ evolution in the face of drug pressure. In particular, our results identify amino acid changes that can be functionally tolerated by $M^{pro}$ that are likely to disrupt binding to inhibitors. In a recent study, Shaqra, Schiffer and colleges mapped the $M^{pro}$ substrate envelope; locations where the inhibitors protrude from this envelope is an indicator of susceptibility to resistance mutations (Shaqra, Zvornicanin et al. 2022). The information in these two studies provides a new view into resistance evolution that can be incorporated into ongoing drug design efforts. Locations in the active site as well as at a likely allosteric site that cannot readily evolve without compromising function are ideal targets for anchoring inhibitors with reduced potential to evolve drug resistance.

Our next steps involve developing efficient strategies for assaying $M^{pro}$ fitness landscapes in the presence of potential inhibitors in order to define structure-resistance relationships. This would provide critical guidance for reducing the likelihood of resistance at earlier stages of drug development than is currently possible. For example, it would identify inhibitors with the least likelihood of developing resistance. It would also provide the potential for identifying inhibitors with non-overlapping resistance profiles that if used in combination would not be susceptible to resistance from an individual mutation. There are technical hurdles to overcome in using our yeast-based screens to investigate resistance because many small-molecules are ineffective due to poor permeability and/or export from yeast. We are assessing strategies to both increase the druggability of yeast and porting our assays to mammalian cells (Chinen, Hamada et al. 2017). The results from our current work on $M^{pro}$ in yeast as well as previous studies using fitness landscapes to analyze drug resistance in other proteins (Deng, Huang et al. 2012, Choi, Landrette et al. 2014, Firnberg, Labonte et al. 2014, Ma, Boucher et al.

2017) indicates a strong potential of these approaches to improve our understanding and ability to
472 combat resistance evolution.

474

476

# Materials and methods

## Construction of WT Ub-M$^{pro}$ vector (p416LexA_UbM$^{pro}$(WT)_B112)

The Ubiqutin-M$^{pro}$ gene fusion was constructed using overlapping PCR of the yeast ubiquitin gene and SARS-CoV-2 M$^{pro}$ gene (Jin, Du et al. 2020) and was inserted into the pRS416 vector after digestion with SpeI and BamHI. Four LexA boxes were amplified from the LexAbox4_citrine plasmid (FRP793_insul-(lexA-box)4-PminCYC1-Citrine-TCYC1 was a gift from Joerg Stelling; Addgene plasmid # 58434; http://n2t.net/addgene:58434)(Ottoz, Rudolf et al. 2014) and inserted between the SacI and SpeI sites upstream of the ubiquitin-M$^{pro}$ gene. The LexA_ER_B112 transcription factor was amplified from Addgene_58437 (FRP880_PACT1(-1-520)-LexA-ER-haB112-TCYC1 was a gift from Joerg Stelling; Addgene plasmid # 58437; http://n2t.net/addgene:58437)(Ottoz, Rudolf et al. 2014) and inserted into the KpnI site. The resulting vector is named (p416LexA-UbM$^{pro}$(WT)-B112). A destination vector was generated by removing the M$^{pro}$ sequence and replacing it with a restriction site for SphI.

## Generating mutant libraries

The SARS-CoV-2 M$^{pro}$ (ORF1ab polyprotein residues 3264-3569, GenBank code: MN908947.3) single site variant library was synthesized by Twist Biosciences (twistbioscience.com) by massively parallel oligonucleotide synthesis. In the library, each amino acid position was modified to all 19 amino acid variants plus a premature termination encoded by a stop codon, using the preferred yeast codon for each substitution. All 306 amino acids of M$^{pro}$ were modified yielding 6120 total variants. Due to challenges in construction, positions 27 and 28 were missing from the library. 35 bp of sequence homologous to the destination vector was added to both termini of the library during synthesis to enable efficient cloning. The library was combined via Gibson assembly (NEB) with the destination vector. To avoid bottlenecking the library, sufficient transformations were performed to recover more than 50 independent transformants for each designed M$^{pro}$ variant in the library. To improve efficiency and accuracy of deep sequencing steps during bulk competition, each variant of the library was tagged with a unique barcode. A pool of DNA constructs containing a randomized 18 bp barcode sequence (N18) was cloned into the NotI and AscI sites upstream of the LexA promoter sequence via restriction digestion, ligation and transformation into chemically competent E. *coli*. These experiments were performed at a scale designed to have each M$^{pro}$ variant represented by 10-20 unique barcodes. The resulting library is named p416LexA-UbM$^{pro}$(lib)-B112.

## Barcode association

To associate barcodes with $M^{pro}$ variants, we digested the p416-Ub$M^{pro}$(lib)-B112 plasmid upstream of the N18 sequence and downstream of the $M^{pro}$ sequence with NotI and SalI enzymes (NEB). The resulting 1800 bp fragment containing the barcoded library was isolated by Blue Pippen selecting for a 1 to 4 kB range. Of note, we determined it was important to avoid PCR to prepare the DNA for PacBio sequencing, as PCR led to up to 25% of DNA strands recombining, leading to widespread mismatch between the barcode and $M^{pro}$ variant. DNA was prepared for sequencing with the Sequel II Binding Kit v2.1 and the libraries were sequenced on a Pacific Biosciences Sequel II Instrument using a 15-hour data collection time, with a 0.4-hour pre-extension time (PacBio Core Enterprise, UMass Chan Medical School, Worcester, MA). PacBio circular consensus sequences (CCS) were generated from the raw reads using SMRTLink v.10.1 and standard Read-Of-Insert (ROI) analysis parameters. After filtering low-quality reads (Phred scores < 10), the data was organized by barcode sequence using custom analysis scripts that are available upon request. For each barcode that was read more than three times, we generated a consensus of the $M^{pro}$ sequence that we compared to WT to call mutations.

As a control for library experiments, the WT Ub-$M^{pro}$ gene was also barcoded with approximately 150 unique barcode sequences. The randomized 18 bp barcode sequence (N18) was cloned between the NotI and AscI sites upstream of the LexA promoter sequence in the p416LexA-Ub-$M^{pro}$(WT)-B112 vector with the goal of the WT sequence being represented by approximately 100 barcodes. The barcoded region of the plasmid was amplified by PCR using the primers listed in Table S1 (for the WT barcoding it was not necessary to avoid strand recombination) and sequenced by EZ Amplicon deep sequencing (www.genewiz.com).

**Generating split transcription factor strain**

The GFP reporter strain was generated by integration of GFP driven by a Gal1 promoter together with a HIS3 marker into the HO genomic locus. The Gal4, Gal80 and Pdr5 genes were disrupted to create the following strain: W303 *HO::Gal1-GFP-v5-His3; gal4::trp1; gal80::leu2 pdr5::natMX*.

The Gal4 DNA binding domain-$M^{pro}$CS-activation domain fusion gene (DBD-$M^{pro}$CS-AD) was generated by overlapping PCR. The Gal4 DNA binding domain (DBD) was amplified by PCR with a forward primer containing the EcoRI site and a reverse primer containing the extending $M^{pro}$CS overhang sequence. The Gal4 activation domain (AD) was amplified by PCR with a forward primer containing the $M^{pro}$CS overhang sequence and a reverse primer containing the SacI site (SacI_R). The DBD-$M^{pro}$CS-AD fusion gene was generated using the overlapping DBD-$M^{pro}$CS and $M^{pro}$CS-AD products from above as templates and the EcoRI_F and SacI_R primers. The resulting DBD-$M^{pro}$CS-AD fusion gene was inserted between the EcoRI and SacI sites downstream of the CUP promoter in the integrative bidirectional pDK-ATC plasmid (kindly provided by D. Kaganovich)(Amen and Kaganovich 2017). The mCherry gene was subsequently cloned into the XhoI/BamHI sites downstream of the TEF promoter in the opposite orientation to create the plasmid pDK-CUP-DBD-$M^{pro}$CS-AD-TEF-mCherry. The fragment for genomic integration was generated by PCR with the primers listed in Table S1, was transformed into the

reporter stain using LiAc/PEG transformation (Gietz, Schiestl et al. 1995), and successful integration of the module into the adenine biosynthesis gene was verified by PCR.

**Bulk Split transcription factor (TF) competition experiment**

Barcoded WT UbM$^{pro}$ (p416LexA-UbM$^{pro}$(WT)-N18) plasmid was mixed with the barcoded UbM$^{pro}$ library (p416LexA-UbM$^{pro}$(lib)-N18) at a ratio of 20-fold WT to the average library variant. The blended plasmid library was transformed using the lithium acetate procedure into the reporter strain (*W303 ade::CUP-DBD-M$^{pro}$CS-AD-TEF-mCherry; ho::gal1-gfp-v5-his3; gal4::trp1; gal80::leu2; pdr5::natMX*). Sufficient transformation reactions were performed to attain about 5 million independent yeast transformants representing a 50-fold sampling of the average barcode. Each biological replicate represents a separate transformation of the library. Following 12 hours of recovery in synthetic dextrose lacking adenine (SD-A), transformed cells were washed three times in SD-A-U media (SD lacking adenine and uracil to select for the presence of the M$^{pro}$ variant plasmid) to remove extracellular DNA and grown in 500 mL SD-A-U media at 30°C for 48 hours with repeated dilution to maintain the cells in log phase of growth and to expand the library. Subsequently, the library was diluted to early log phase in 100 mL of SD-A-U, grown for two hours, the culture was split in half, and 125 nM β-estradiol (from a 10 mM stock in 95% ethanol) was added to one of the cultures to induce Ub-M$^{pro}$ expression. Cultures with and without β-estradiol were grown with shaking at 180 rpm for 6 hours at which point samples of ~$10^7$ cells were collected for FACS analysis.

**FACS sorting of TF screen yeast cells**

A sample of $10^7$ cells were washed three times with 500 µL of Tris-Buffered Saline containing 0.1% Tween and 0.1% bovine serum albumin (TBST-BSA). Cells were diluted to $10^6$/mL and transferred to polystyrene FACS tubes. Samples were sorted for GFP and mCherry expression on a FACS Aria II cell sorter with all cells expressing cut TF (low GFP expression) in one population and uncut TF (high GFP expression) in a second population. To ensure adequate library coverage, we sorted at least 1.5 million cells of each population and collected them in SD-A-U media. Sorted yeast cells were amplified in 20 mL SD-U-A media for 10 hours at 30°C. These yeast samples were collected by centrifugation and cell pellets were stored at -80°C.

**Generating FRET strain**

The YPet-CyPet FRET pair is a YFP-CFP fluorescent protein pair that has been fluorescently optimized by directed evolution for intracellular FRET (Nguyen and Daugherty 2005). The YPet- M$^{pro}$CS-CyPet fusion gene was generated by overlapping PCR as follows. The CyPet gene was amplified by PCR from the pCyPet-His vector (pCyPet-His was a gift from Patrick Daugherty; Addgene plasmid # 14030 ;

http://n2t.net/addgene:14030) with a forward primer containing the BamHI site (BamHI_F) and a reverse primer containing the extending M$^{pro}$CS overhang sequence. The YPet gene was amplified by PCR from the pYPet-His vector (pYPet-His was a gift from Patrick Daugherty; Addgene plasmid # 14031 ; http://n2t.net/addgene:14031) with a forward primer containing the extending M$^{pro}$CS overhang sequence and a reverse primer containing the XhoI site (XhoI_R). The CyPet-M$^{pro}$CS-YPet fusion gene was generated using the overlapping CyPet-M$^{pro}$CS and M$^{pro}$CS-YPet products from above as templates and BamHI_F and XhoI_R primers. The resulting CyPet- M$^{pro}$CS-YPet gene was inserted between the BamHI and XhoI sites downstream of the TEF promoter in the integrative bidirectional pDK-ATG plasmid (kindly provided by D. Kaganovich)(Amen and Kaganovich 2017). The fragment for genomic integration was generated by PCR with the primers listed in Table S1, was transformed into W303 (*leu2-3,112 trp1-1 can1-100 ura3-1 ade2-1 his3-11,15*) using LiAc/PEG transformation(Gietz, Schiestl et al. 1995), and successful integration of the module into the adenine biosynthesis gene was verified by PCR.

**Bulk FRET competition experiment**

The plasmid library including the barcoded WT plasmid was transformed as above using the lithium acetate procedure into *W303 Ade::TEF-CyPet-M$^{pro}$CS-YPet* cells. Sufficient transformation reactions were performed to attain about 5 million independent yeast transformants representing a 50-fold sampling of the average barcode. Cultures were grown and induced with β-estradiol as above for the transcription factor screen with the exception that cells were induced for 1.5 hours. Samples of $10^7$ cells were collected for FACS analysis.

**FACS sorting of FRET screen yeast cells**

A sample of $10^7$ cells were washed three times with 500 µL of TBST-BSA. Cells were diluted to $10^6$/mL and transferred to polystyrene FACS tubes. Samples were sorted for YFP and CFP expression on a FACS Aria II cell sorter with all cells expressing cut FRET pair (low FRET) in one population and uncut FRET pair (high FRET) in a second population. To ensure adequate library coverage, we sorted at least 3 million cells of each population and collected them in SD-A-U media. Yeast samples were collected by centrifugation and cell pellets were stored at -80°C.

**Growth strain**

The plasmid library including the barcoded WT plasmid was transformed as above using the lithium acetate procedure into W303 cells. Libraries were expanded as for the split TF screen, and then the library was diluted to early log phase in 100 mL of SD-A-U, grown for two hours, the culture was split in half, and 2 µM β-estradiol (from a 10 mM stock in 95% ethanol) was added to one of the cultures to induce Ub-M$^{pro}$ expression. Cultures with and without β-estradiol were grown with shaking at 180 rpm

for 16 hours with dilution after 8 hours to maintain growth in exponential phase. Samples of ~$10^8$ cells were collected by centrifugation and cell pellets were stored at -80°C.

**DNA preparation and sequencing**

We isolated plasmid DNA from each FACS cell population and the time points from the growth experiment as described (Jiang, Mishra et al. 2013). Purified plasmid DNA was linearized with AscI. Barcodes were amplified with 22 cycles of PCR using Phusion polymerase (NEB) and primers that add Illumina adapter sequences and a 6 bp identifier sequence used to distinguish cell populations. PCR products were purified two times over silica columns (Zymo Research) and quantified using the KAPA SYBR FAST qPCR Master Mix (Kapa Biosystems) on a Bio-Rad CFX machine. Samples were pooled and sequenced on an Illumina NextSeq instrument in single-end 75 bp mode.

**Analysis of bulk competition Illumina sequencing data**

We analyzed the Illumina barcode reads using custom scripts that are available upon request. Illumina sequence reads were filtered for Phred scores > 10 and strict matching of the sequence to the expected template and identifier sequence. Reads that passed these filters were parsed based on the identifier sequence. For each screen/cell population, each unique N18 read was counted. The unique N18 count file was then used to identify the frequency of each mutant using the variant-barcode association table. To generate a cumulative count for each codon and amino acid variant in the library, the counts of each associated barcode were summed.

**Determination of selection coefficient**

To determine the functional score for each variant in the two FACS-based screens, the fraction of each variant in the cut and uncut windows was first calculated by dividing the sequencing counts of each variant in a window by the total counts in that window. The functional score was then calculated as the fraction of the variant in the cut window divided by the sum of the fraction of the variant in the cut and uncut windows. The functional score for the growth screen was calculated by the fraction of the variant at the 0 hour time point divided by the sum of the fraction of the variant in the 0 and 16 hour time points.

**Analysis of $M^{pro}$ expression and Ubiquitin removal by Western Blot**

To facilitate analysis of expression levels of $M^{pro}$ and examine effective removal of Ubiquitin, a his tag was fused to the C-terminus of $M^{pro}$ to create the plasmid p416LexA-Ub$M^{pro}$-$his_6$-B112. In addition, the C145A mutation was created by site-directed mutagenesis to ensure cleavage by Ub specific proteases

and to reduce the toxicity caused by WT $M^{pro}$ expression. W303 cells were transformed with the p416LexA-Ub$M^{pro}$(C145A)-his construct and the resulting yeast cells were grown to exponential phase in SD-ura media at 30°C. 125 nM β-estradiol was added when indicated and cells were grown for an additional eight hours. $10^8$ yeast cells were collected by centrifugation and frozen as pellets at −80°C. Cells were lysed by vortexing the thawed pellets with glass beads in lysis buffer (50 mM Tris-HCl pH 7.5, 5 mM EDTA and 10 mM PMSF), followed by addition of 2% Sodium dodecyl sulfate (SDS). Lysed cells were centrifuged at 18,000 g for 1 min to remove debris, and the protein concentration of the supernatants was determined using a BCA protein assay kit (Pierce) compared to a Bovine Serum Albumin (BSA) protein standard. 15 µg of total cellular protein was resolved by SDS-PAGE, transferred to a PVDF membrane, and probed using an anti-his antibody (ref). Purified $M^{pro}$-$his_6$ protein was a gift from the Schiffer laboratory.

### Sequence and structure analysis

Evolutionary conservation was calculated with an alignment of homologs from diverse species using the ConSurf server (Ashkenazy H, Abadi, S.). The effects of single mutations on protein-ligand interactions were predicted by calculating the binding affinity changes using PremPLI (https://lilab.jysw.suda.edu.cn/research/PremPLI/) (Sun, T., Chen Y et al). The figures were generated using Matplotlib (Hunter 2007), PyMOL and GraphPad Prism version 9.3.1.

### Identifying mutations in circulating SARS-COV-2 sequences

The complete set of SARS-COV-2 isolate genome sequences was downloaded from the GISAID database. The SARS-COV-2 $M^{pro}$ reference sequence (NCBI accession NC_045512.2) was used as a query in a tBLASTn search against the translated nucleotide sequences of these isolates to identify the MPro region and its protein sequence for each isolate, if present. Mpro sequences were discarded if they contained 10 or more ambiguous “X” amino acids, or had amino acid length less than 290. A multiple sequence alignment was performed and for each of the twenty standard amino acids, the number of times it was observed at each position in the MPro sequence was calculated.

## Acknowledgements

This work was sponsored by Novartis Institutes for BioMedical Research. We would like to thank the UMass Chan Medical School Pacific Biosciences Core Enterprise for providing the PacBio NGS services and the UMass Chan Medical School Flow Cytometry Core Facility for providing the FACS services. We would also like to thank Ala Shaqra, Sarah Zvornicanin, and Qiu Yu Huang for conceptual discussions of the manuscript.

## Competing interests

DTB, SAM, and DD are employees of Novartis Institutes for Biomedical Research

# References


Alalam, H., S. Sigurdardottir, C. Bourgard, I. Tiukova, R. D. King, M. Grotli and P. Sunnerhagen (2021). "A Genetic Trap in Yeast for Inhibitors of SARS-CoV-2 Main Protease." mSystems: e0108721.

Amen, T. and D. Kaganovich (2017). "Integrative modules for efficient genome engineering in yeast." Microb Cell **4**(6): 182-190.

Bachmair, A., D. Finley and A. Varshavsky (1986). "In vivo half-life of a protein is a function of its amino-terminal residue." Science **234**(4773): 179-186.

Barrila, J., U. Bacha and E. Freire (2006). "Long-range cooperative interactions modulate dimerization in SARS 3CLpro." Biochemistry **45**(50): 14908-14916.

Bhat, Z. A., D. Chitara, J. Iqbal, B. S. Sanjeev and A. Madhumalar (2021). "Targeting allosteric pockets of SARS-CoV-2 main protease M(pro)." J Biomol Struct Dyn: 1-16.

Biering, S. B., E. Van Dis, E. Wehri, L. H. Yamashiro, X. Nguyenla, C. Dugast-Darzacq, T. G. W. Graham, J. R. Stroumza, G. R. Golovkine, A. W. Roberts, D. M. Fines, J. N. Spradlin, C. C. Ward, T. Bajaj, D. Dovala, U. Schulze-Gamen, R. Bajaj, D. M. Fox, M. Ott, N. Murthy, D. K. Nomura, J. Schaletzky and S. A. Stanley (2021). "Screening a Library of FDA-Approved and Bioactive Compounds for Antiviral Activity against SARS-CoV-2." ACS Infect Dis **7**(8): 2337-2351.

Boucher, J. I., D. N. A. Bolon and D. S. Tawfik (2019). "Quantifying and understanding the fitness effects of protein mutations: Laboratory versus nature." Protein Sci **28**(3): 671.

Bzowka, M., K. Mitusinska, A. Raczynska, A. Samol, J. A. Tuszynski and A. Gora (2020). "Structural and Evolutionary Analysis Indicate That the SARS-CoV-2 Mpro Is a Challenging Target for Small-Molecule Inhibitor Design." Int J Mol Sci **21**(9).

Chen, S., J. Zhang, T. Hu, K. Chen, H. Jiang and X. Shen (2008). "Residues on the dimer interface of SARS coronavirus 3C-like protease: dimer stability characterization and enzyme catalytic activity analysis." J Biochem **143**(4): 525-536.

Cheng, S. C., G. G. Chang and C. Y. Chou (2010). "Mutation of Glu-166 blocks the substrate-induced dimerization of SARS coronavirus main protease." Biophys J **98**(7): 1327-1336.

Chinen, T., K. Hamada, A. Taguchi, Y. Asami, K. Shiomi, Y. Hayashi and T. Usui (2017). Multidrug Sensitive Yeast Strains, Useful Tools for Chemical Genetics. The Yeast Role in Medical Applications. W. M. H. Abdulkhair.

Cho, E., M. Rosa, R. Anjum, S. Mehmood, M. Soban, M. Mujtaba, K. Bux, S. T. Moin, M. Tanweer, S. Dantu, A. Pandini, J. Yin, H. Ma, A. Ramanathan, B. Islam, A. Mey, D. Bhowmik and S. Haider (2021). "Dynamic Profiling of beta-Coronavirus 3CL M(pro) Protease Ligand-Binding Sites." J Chem Inf Model **61**(6): 3058-3073.

Choi, J., S. F. Landrette, T. Wang, P. Evans, A. Bacchiocchi, R. Bjornson, E. Cheng, A. L. Stiegler, S. Gathiaka, O. Acevedo, T. J. Boggon, M. Krauthammer, R. Halaban and T. Xu (2014). "Identification of PLX4032-resistance mechanisms and implications for novel RAF inhibitors." Pigment Cell Melanoma Res **27**(2): 253-262.

Chou, C. Y., H. C. Chang, W. C. Hsu, T. Z. Lin, C. H. Lin and G. G. Chang (2004). "Quaternary structure of the severe acute respiratory syndrome (SARS) coronavirus main protease." Biochemistry **43**(47): 14958-14970.

Deng, Z., W. Huang, E. Bakkalbasi, N. G. Brown, C. J. Adamski, K. Rice, D. Muzny, R. A. Gibbs and T. Palzkill (2012). "Deep sequencing of systematic combinatorial libraries reveals beta-lactamase sequence constraints at high resolution." J Mol Biol **424**(3-4): 150-167.

Edwards, C. E., B. L. Yount, R. L. Graham, S. R. Leist, Y. J. Hou, K. H. Dinnon, 3rd, A. C. Sims, J. Swanstrom, K. Gully, T. D. Scobey, M. R. Cooley, C. G. Currie, S. H. Randell and R. S. Baric (2020). "Swine acute diarrhea syndrome coronavirus replication in primary human cells reveals potential susceptibility to infection." Proc Natl Acad Sci U S A **117**(43): 26915-26925.

Estrada, E. (2020). "Topological analysis of SARS CoV-2 main protease." Chaos **30**(6): 061102.

Firnberg, E., J. W. Labonte, J. J. Gray and M. Ostermeier (2014). "A comprehensive, high-resolution map of a gene's fitness landscape." Mol Biol Evol **31**(6): 1581-1592.

Fischer, C., N. A. Veprek, Z. Peitsinis, K. Ruhmann, C. Yang, J. N. Spradlin, D. Dovala, D. K. Nomura, Y. Zyang and F. Trauner (2021). "*De novo* Design of SARS-CoV-2 Main Protease Inhibitors." Synlett: https:/doi.org/10.1055/a-1582-0243.

Fowler, D. M. and S. Fields (2014). "Deep mutational scanning: a new style of protein science." Nat Methods **11**(8): 801-807.

Gietz, R. D., R. H. Schiestl, A. R. Willems and R. A. Woods (1995). "Studies on the transformation of intact yeast cells by the LiAc/SS-DNA/PEG procedure." Yeast **11**(4): 355-360.

Hegyi, A., A. Friebe, A. E. Gorbalenya and J. Ziebuhr (2002). "Mutational analysis of the active centre of coronavirus 3C-like proteases." J Gen Virol **83**(Pt 3): 581-593.

Heinrich, R. and T. A. Rapoport (1974). "A linear steady-state treatment of enzymatic chains. General properties, control and effector strength." Eur J Biochem **42**(1): 89-95.

Hietpas, R. T., J. D. Jensen and D. N. Bolon (2011). "Experimental illumination of a fitness landscape." Proc Natl Acad Sci U S A **108**(19): 7896-7901.

Hsu, W. C., H. C. Chang, C. Y. Chou, P. J. Tsai, P. I. Lin and G. G. Chang (2005). "Critical assessment of important regions in the subunit association and catalytic action of the severe acute respiratory syndrome coronavirus main protease." J Biol Chem **280**(24): 22741-22748.

Hunter, J. D. (2007). ""Matplotlib: A 2D Graphics Environment"." Computing in Science and Engineering **9**(3): 90-95.

Jiang, L., P. Mishra, R. T. Hietpas, K. B. Zeldovich and D. N. Bolon (2013). "Latent effects of Hsp90 mutants revealed at reduced expression levels." PLoS Genet **9**(6): e1003600.

Jin, Z., X. Du, Y. Xu, Y. Deng, M. Liu, Y. Zhao, B. Zhang, X. Li, L. Zhang, C. Peng, Y. Duan, J. Yu, L. Wang, K. Yang, F. Liu, R. Jiang, X. Yang, T. You, X. Liu, X. Yang, F. Bai, H. Liu, X. Liu, L. W. Guddat, W. Xu, G. Xiao, C. Qin, Z. Shi, H. Jiang, Z. Rao and H. Yang (2020). "Structure of M(pro) from SARS-CoV-2 and discovery of its inhibitors." Nature **582**(7811): 289-293.

Johnston, S. A., M. J. Zavortink, C. Debouck and J. E. Hopper (1986). "Functional domains of the yeast regulatory protein GAL4." Proc Natl Acad Sci U S A **83**(17): 6553-6557.

Kacser, H. and D. A. Fell (1995). "The control of flux: 21 years on." Biochemical Society Transactions **23**(2): 341-366.

Kneller, D. W., G. Phillips, H. M. O'Neill, R. Jedrzejczak, L. Stols, P. Langan, A. Joachimiak, L. Coates and A. Kovalevsky (2020). "Structural plasticity of SARS-CoV-2 3CL M(pro) active site cavity revealed by room temperature X-ray crystallography." Nat Commun **11**(1): 3202.

Ksiazek, T. G., D. Erdman, C. S. Goldsmith, S. R. Zaki, T. Peret, S. Emery, S. Tong, C. Urbani, J. A. Comer, W. Lim, P. E. Rollin, S. F. Dowell, A. E. Ling, C. D. Humphrey, W. J. Shieh, J. Guarner, C. D. Paddock, P. Rota, B. Fields, J. DeRisi, J. Y. Yang, N. Cox, J. M. Hughes, J. W. LeDuc, W. J. Bellini, L. J. Anderson and S. W. Group (2003). "A novel coronavirus associated with severe acute respiratory syndrome." N Engl J Med **348**(20): 1953-1966.

Lin, P. Y., C. Y. Chou, H. C. Chang, W. C. Hsu and G. G. Chang (2008). "Correlation between dissociation and catalysis of SARS-CoV main protease." Arch Biochem Biophys **472**(1): 34-42.

Ma, L., J. I. Boucher, J. Paulsen, S. Matuszewski, C. A. Eide, J. Ou, G. Eickelberg, R. D. Press, L. J. Zhu, B. J. Druker, S. Branford, S. A. Wolfe, J. D. Jensen, C. A. Schiffer, M. R. Green and D. N. Bolon (2017). "CRISPR-Cas9-mediated saturated mutagenesis screen predicts clinical drug resistance with improved accuracy." Proc Natl Acad Sci U S A **114**(44): 11751-11756.

MacDonald, E. A., G. Frey, M. N. Namchuk, S. C. Harrison, S. M. Hinshaw and I. W. Windsor (2021). "Recognition of Divergent Viral Substrates by the SARS-CoV-2 Main Protease." ACS Infect Dis **7**(9): 2591-2595.

Melamed, D., D. L. Young, C. E. Gamble, C. R. Miller and S. Fields (2013). "Deep mutational scanning of an RRM domain of the Saccharomyces cerevisiae poly(A)-binding protein." RNA **19**(11): 1537-1551.

Meyer, B., J. Chiaravalli, S. Gellenoncourt, P. Brownridge, D. P. Bryne, L. A. Daly, A. Grauslys, M. Walter, F. Agou, L. A. Chakrabarti, C. S. Craik, C. E. Eyers, P. A. Eyers, Y. Gambin, A. R. Jones, E. Sierecki, E. Verdin, M. Vignuzzi and E. Emmott (2021). "Characterising proteolysis during SARS-CoV-2 infection identifies viral cleavage sites and cellular targets with therapeutic potential." Nat Commun **12**(1): 5553.

Mishra, P., J. M. Flynn, T. N. Starr and D. N. A. Bolon (2016). "Systematic Mutant Analyses Elucidate General and Client-Specific Aspects of Hsp90 Function." Cell Rep **15**(3): 588-598.

Murray, M. G., W. Hung, I. Sadowski and B. Das Mahapatra (1993). "Inactivation of a yeast transactivator by the fused HIV-1 proteinase: a simple assay for inhibitors of the viral enzyme activity." Gene **134**(1): 123-128.

Nguyen, A. W. and P. S. Daugherty (2005). "Evolutionary optimization of fluorescent proteins for intracellular FRET." Nat Biotechnol **23**(3): 355-360.

Ohta, T. (1973). "Slightly deleterious mutant substitutions in evolution." Nature **246**(5428): 96-98.

Ottoz, D. S., F. Rudolf and J. Stelling (2014). "Inducible, tightly regulated and growth condition-independent transcription factor in Saccharomyces cerevisiae." Nucleic Acids Res **42**(17): e130.

Owen, D. R., C. M. N. Allerton, A. S. Anderson, L. Aschenbrenner, M. Avery, S. Berritt, B. Boras, R. D. Cardin, A. Carlo, K. J. Coffman, A. Dantonio, L. Di, H. Eng, R. Ferre, K. S. Gajiwala, S. A. Gibson, S. E. Greasley, B. L. Hurst, E. P. Kadar, A. S. Kalgutkar, J. C. Lee, J. Lee, W. Liu, S. W. Mason, S. Noell, J. J. Novak, R. S. Obach, K. Ogilvie, N. C. Patel, M. Pettersson, D. K. Rai, M. R. Reese, M. F. Sammons, J. G. Sathish, R. S. P. Singh, C. M. Steppan, A. E. Stewart, J. B. Tuttle, L. Updyke, P. R. Verhoest, L. Wei, Q. Yang and Y. Zhu (2021). "An oral SARS-CoV-2 M(pro) inhibitor clinical candidate for the treatment of COVID-19." Science: eabl4784.

Roscoe, B. P., K. M. Thayer, K. B. Zeldovich, D. Fushman and D. N. Bolon (2013). "Analyses of the effects of all ubiquitin point mutants on yeast growth rate." J Mol Biol **425**(8): 1363-1377.

Shaqra, A. M., S. Zvornicanin, Q. Y. Huang, G. J. Lockbaum, M. Knapp, L. Tandeske, D. T. Barkan, J. M. Flynn, D. N. A. Bolon, S. Moquin, D. Dovala, N. K. Yilmaz and C. A. Schiffer (2022). "Defining the Substrate Envelope of SARS-CoV-2 Main Protease to Predict and Avoid Drug Resistance." bioRixv, doi: https/doi.org/10.1101/2022.01.25.477757.

Singer, J., R. Gifford, M. Cotten and D. Robertson (2020). "CoV-GLUE: A Web Application for Tracking SARS-CoV-2 Genomic Variation." Preprints

Singh, J., R. C. Petter, T. A. Baillie and A. Whitty (2011). "The resurgence of covalent drugs." Nat Rev Drug Discov **10**(4): 307-317.

Starita, L. M., J. N. Pruneda, R. S. Lo, D. M. Fowler, H. J. Kim, J. B. Hiatt, J. Shendure, P. S. Brzovic, S. Fields and R. E. Klevit (2013). "Activity-enhancing mutations in an E3 ubiquitin ligase identified by high-throughput mutagenesis." Proc Natl Acad Sci U S A **110**(14): E1263-1272.

Tan, J., K. H. Verschueren, K. Anand, J. Shen, M. Yang, Y. Xu, Z. Rao, J. Bigalke, B. Heisen, J. R. Mesters, K. Chen, X. Shen, H. Jiang and R. Hilgenfeld (2005). "pH-dependent conformational flexibility of the SARS-CoV main proteinase (M(pro)) dimer: molecular dynamics simulations and multiple X-ray structure analyses." J Mol Biol **354**(1): 25-40.

Thiel, V., K. A. Ivanov, A. Putics, T. Hertzig, B. Schelle, S. Bayer, B. Weissbrich, E. J. Snijder, H. Rabenau, H. W. Doerr, A. E. Gorbalenya and J. Ziebuhr (2003). "Mechanisms and enzymes involved in SARS coronavirus genome expression." J Gen Virol **84**(Pt 9): 2305-2315.

Weng, Y. L., S. R. Naik, N. Dingelstad, M. R. Lugo, S. Kalyaanamoorthy and A. Ganesan (2021). "Molecular dynamics and in silico mutagenesis on the reversible inhibitor-bound SARS-CoV-2 main protease complexes reveal the role of lateral pocket in enhancing the ligand affinity." Sci Rep **11**(1): 7429.

Xue, X., H. Yang, W. Shen, Q. Zhao, J. Li, K. Yang, C. Chen, Y. Jin, M. Bartlam and Z. Rao (2007). "Production of authentic SARS-CoV M(pro) with enhanced activity: application as a novel tag-cleavage endopeptidase for protein overproduction." J Mol Biol **366**(3): 965-975.

Zaki, A. M., S. van Boheemen, T. M. Bestebroer, A. D. Osterhaus and R. A. Fouchier (2012). "Isolation of a novel coronavirus from a man with pneumonia in Saudi Arabia." N Engl J Med **367**(19): 1814-1820.

Zhang, L., D. Lin, X. Sun, U. Curth, C. Drosten, L. Sauerhering, S. Becker, K. Rox and R. Hilgenfeld (2020). "Crystal structure of SARS-CoV-2 main protease provides a basis for design of improved alpha-ketoamide inhibitors." Science **368**(6489): 409-412.

Zhao, Y., C. Fang, Q. Zhang, R. Zhang, X. Zhao, Y. Duan, H. Wang, Y. Zhu, L. Feng, J. Zhao, M. Shao, X. Yang, L. Zhang, C. Peng, K. Yang, D. Ma, Z. Rao and H. Yang (2021). "Crystal structure of SARS-CoV-2 main protease in complex with protease inhibitor PF-07321332." Protein Cell.